Hyperbolic Dehn filling in dimension four

BRUNO MARTELLI

STEFANO RIOLO

We introduce and study some deformations of complete finite-volume hyperbolic four-manifolds that may be interpreted as four-dimensional analogues of Thurston's hyperbolic Dehn filling.

We construct in particular an analytic path of complete, finite-volume cone four-manifolds M_t that interpolates between two hyperbolic four-manifolds M_0 and M_1 with the same volume $\frac{8}{3}\pi^2$. The deformation looks like the familiar hyperbolic Dehn filling paths that occur in dimension three, where the cone angle of a core simple closed geodesic varies monotonically from 0 to 2π. Here, the singularity of M_t is an immersed geodesic surface whose cone angles also vary monotonically from 0 to 2π. When a cone angle tends to 0 a small core surface (a torus or Klein bottle) is drilled, producing a new cusp.

We show that various instances of hyperbolic Dehn fillings may arise, including one case where a degeneration occurs when the cone angles tend to 2π, like in the famous figure-eight knot complement example.

The construction makes an essential use of a family of four-dimensional deforming hyperbolic polytopes recently discovered by Kerckhoff and Storm.

1 Introduction

By Mostow–Prasad rigidity [21; 22], complete finite-volume hyperbolic manifolds can be deformed only in dimension two. Some deformations may arise also in higher dimension if one works in the more general setting of *hyperbolic cone manifolds*: the celebrated Thurston hyperbolic Dehn filling theorem states that every cusped hyperbolic three-manifold may be deformed to a hyperbolic cone manifold, whose singular locus consists of small simple closed geodesics with small cone angles. As the deformation goes on, both the geodesic length and the cone angle increase: if the cone angle reaches 2π we get a genuine hyperbolic manifold without singularities.

The aim of this paper is to show that this phenomenon occurs sometimes also in dimension four. We prove this by constructing some examples explicitly.

Hyperbolic cone manifolds

Hyperbolic cone manifolds were defined in every dimension by Thurston [26]; see also Boileau, Leeb and Porti [3], Cooper, Hodgson and Kerckhoff [5] and McMullen [18]. Hyperbolic cone surfaces and three-manifolds are widely studied; see for instance Bromberg [4], Hodgson and Kerckhoff [11], Kojima [14], Mazzeo and Montcouquiol [17] and Weiss [28; 29]. The singular locus in an orientable hyperbolic cone three-manifold consists of closed geodesics or more complicated graphs. Not much seems to be known in dimension four or higher.

We construct here some hyperbolic cone four-manifolds M whose singular locus Σ is the image of a (possibly disconnected) geodesically immersed hyperbolic cone surface $i\colon \widetilde{\Sigma} \looparrowright M$ that self-intersects orthogonally at its cone points. This seems a natural kind of hyperbolic cone four-manifold to study; see Section 2.3 for a precise definition. The image of every connected component of $\widetilde{\Sigma}$ has some cone angle in M, and at each double point $p \in \Sigma$ two components of $\widetilde{\Sigma}$ with (possibly different) cone angles α and β meet orthogonally. Note that every component of $\widetilde{\Sigma}$ is a hyperbolic cone surface and as such it can also be topologically a sphere or a torus.

Main result

The main result of this paper is Theorem 1.1 below. It shows a number of new phenomena. First, it shows that complete finite-volume hyperbolic cone four-manifolds with singular locus a geodesically immersed surface exist. Then, it shows that these cone manifolds can sometimes be deformed, via a deformation that varies the cone angles of the strata, like in dimensions two and three. Finally, it displays an example where the deformation can be carried in both directions until a torus or Klein bottle is drilled, interpolating between two cusped hyperbolic four-manifolds. Such a deformation may be interpreted as a four-dimensional hyperbolic Dehn filling (at both endpoints of the deformation path).

Theorem 1.1 *There is a compact smooth nonorientable four-manifold M with ∂M diffeomorphic to a three-torus, which contains a smooth two-torus and a smooth Klein bottle $T, K \subset \mathrm{int}(M)$, both with trivial normal bundle, that intersect transversely in two points (see Figure 1), such that the following holds.*

There is an analytic path $\{M_t\}_{t\in(0,1)}$ of complete finite-volume hyperbolic cone manifold structures on $\mathrm{int}(M)$ with singular locus the immersed geodesic cone surface
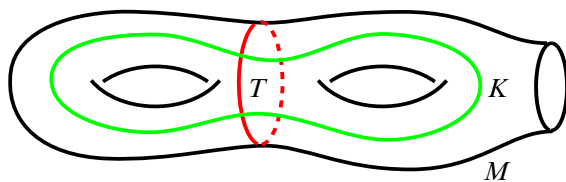
Figure 1: A schematic picture of M and the immersed surface $\Sigma = T \cup K$

$\Sigma = T \cup K$. The two cone surfaces T and K have cone angles $0 < \alpha < 2\pi$ and $0 < \beta < 2\pi$, respectively. We have

$$\text{Area}(T) = 4\pi - 2\beta, \quad \text{Area}(K) = 4\pi - 2\alpha.$$
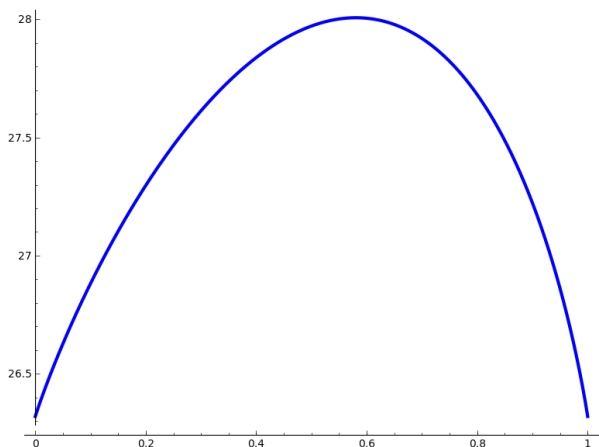
When t varies from 0 to 1 the angle α goes from 0 to 2π and β goes from 2π to 0. The path converges as $t \to 0$ and $t \to 1$ to two complete, finite-volume hyperbolic four-manifolds $M_0 = \text{int}(M) \setminus T$ and $M_1 = \text{int}(M) \setminus K$.

The deformation interpolates analytically between two cusped hyperbolic four-manifolds M_0 and M_1. In contrast to M_t with $t \in (0, 1)$, the manifolds M_0 and M_1 are genuine hyperbolic manifolds, with no cone singularities. The boundary three-torus ∂M gives rise to a cusp in M_t for all $t \in [0, 1]$ diffeomorphic to $S^1 \times S^1 \times S^1 \times [0, +\infty)$ whose Euclidean shape varies with t. The manifolds M_0 and M_1 have also one additional cusp each, obtained by drilling T or K, respectively, whose Euclidean section is diffeomorphic to $T \times S^1$ or $K \times S^1$.

We recall that an important theorem of Garland and Raghunathan [9] implies that the holonomy of a complete finite-volume hyperbolic n–manifold cannot be perturbed when $n \geq 4$. Of course, we are not violating this theorem here, because the holonomy that is moving is that of the *noncomplete* hyperbolic manifold $M \setminus (T \cup K)$. When we say that the deformation varies analytically, we mean that this holonomy does.

The overall picture has some evident similarities with some familiar two- and three-dimensional deformations. The interpolation looks like an analytic path in the moduli or Teichmüller space of a surface connecting two points at infinity, where two intersecting simple closed curves as in Figure 1 are shrunk in opposite directions of the path.

If we look at the deformation by starting at one extreme $t_0 = 0$ or $t_0 = 1$ and moving t towards the other extreme $t_1 = 1 - t_0$, we get a hyperbolic Dehn filling path as in dimension three: the topology of the manifold is modified as soon as we move away from t_0 by a topological Dehn filling (we close a cusp by adding a two-torus or a

Figure 2: The function $\mathrm{Vol}(M_t)$

Klein bottle), and the metric changes by adding a small core geodesic cone surface $S_{t_0} \in \{T, K\}$ with small cone angle. The deformation can be pursued until, at time $1 - t_0$, the core geodesic cone surface S_{t_0} reaches a cone angle of 2π. At the same time the other cone surface S_{t_1} disappears and the two cone points of S_{t_0} become two cusps.

The manifolds M_0 and M_1 have the same small Euler characteristic $\chi = 2$, and hence the same volume

$$\mathrm{Vol}(M_0) = \mathrm{Vol}(M_1) = \frac{8\pi^2}{3}.$$

The volume of M_t is easily expressed in terms of the cone angles α and β as

$$\mathrm{Vol}(M_t) = \frac{8\pi^2}{3}\left(2 - \frac{\alpha + \beta}{2\pi} + \frac{\alpha\beta}{4\pi^2}\right).$$

The volume of M_t is shown in Figure 2. In contrast to dimension three, in our case the volume *increases* under hyperbolic Dehn filling (at both endpoints of the deformation path).

The manifolds M_0 and M_1 are clearly not diffeomorphic; we show that they are not even commensurable: the manifold M_0 is commensurable with the integral lattice in $O(4, 1)$, and M_1 appears to be at the time of writing the smallest known hyperbolic four-manifold that is not commensurable with that lattice. Both manifolds are arithmetic. More recently, some more examples have been constructed by Riolo and Slavich [23], using Slavich [24]. We can in fact interpret M_1 as a new hyperbolic manifold constructed by deforming M_0. It would be interesting to understand in more generality

whether one can vary the cone angles along immersed geodesic cone surfaces in hyperbolic cone four-manifolds, as a tool to construct new hyperbolic manifolds. Some infinitesimal rigidity and existence results were obtained by Montcouquiol [19; 20] for (nonsingular) closed surfaces in the wider context of Einstein deformations.

We note that the manifolds M_t that we construct here are nonorientable. One may build a similar family of orientable deforming cone manifolds by taking the orientable double cover $\widetilde{M}_t$. The cone surfaces T and K lift to three cone tori in $\widetilde{M}_t$, two of cone angle α lying above T and one of cone angle β above K. The manifolds $\widetilde{M}_0$ and $\widetilde{M}_1$ have three and two cusps, respectively, all of three-torus type.

Sketch of the proof

Theorem 1.1 is proved by constructing the family of hyperbolic cone manifolds M_t explicitly.

The construction goes as follows. The fundamental ingredient is a deforming family $\mathcal{F}_t \subset \mathbb{H}^4$ of infinite-volume polytopes built by Kerckhoff and Storm [13]. We truncate here $\mathcal{F}_t$ via two additional hyperplanes to get a deforming family of *finite*-volume polytopes $P_t \subset \mathbb{H}^4$. These polytopes are quite remarkable, because they have for all times t only few nonright dihedral angles. In particular, for the times t that are relevant for the proof of Theorem 1.1, the (two-dimensional) faces with nonright dihedral angles intersect pairwise only at some vertices.

The family P_t interpolates between two Coxeter polytopes of the same volume: the familiar ideal right-angled 24–cell and another interesting polytope with dihedral angles $\frac{\pi}{2}$ and $\frac{\pi}{3}$. We then employ some mirroring and assembling techniques similar to those used by Kolpakov and Martelli [15] to promote each polytope P_t to a hyperbolic cone manifold M_t. Since P_t has few nonright dihedral angles, the manifold M_t has few controlled singularities.

More hyperbolic Dehn fillings

In the Dehn fillings that we have considered in Theorem 1.1, the cusp shape is a flat three-manifold that fibres over a torus or a Klein bottle, and the filling collapses the S^1 fibres. In the deforming cone manifolds context, more different kinds of Dehn fillings may arise that are also interesting. For instance, one may close a cusp of type $S^1 \times S^1 \times S^1$ by collapsing a $S^1 \times S^1$ factor: in this case we add a closed curve

instead of a two-torus, and the resulting space is not a topological manifold. This kind of topological Dehn filling was considered by Fujiwara and Manning [7; 8].

Another variation occurs when the Euclidean cusp section is not a three-torus. For instance, a Euclidean cusp section of a hyperbolic cone four-manifold may be one of the types

$$S^2 \times S^1, \quad S^3,$$

where we see S^n as the *Euclidean* cone manifold obtained by doubling the regular Euclidean n–simplex along its boundary. In this case one may Dehn fill this cusp by collapsing one of the spheres S^1, S^2 or S^3. This corresponds to adding a core S^2, S^1 or a couple of points.

We will show in this paper that all the examples of Dehn fillings mentioned in the above paragraphs arise geometrically as hyperbolic Dehn fillings of some hyperbolic cone manifolds. It is also possible to perform a hyperbolic Dehn *surgery*, the concatenation of a hyperbolic drilling and a hyperbolic filling along an analytic path, that substitutes a small geodesic S^k with a small geodesic S^{3-k}. Topologically, this is just the usual surgery along k–spheres with trivial normal bundles, that is, the substitution of a $S^k \times D^{4-k}$ with a $D^{k+1} \times S^{3-k}$. See Theorem 1.2 below.
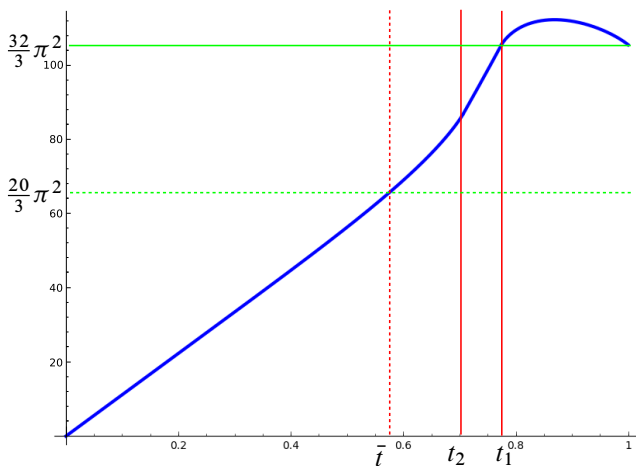
Degeneration

An important phenomenon in dimension three, first described by Thurston [25], is that of a hyperbolic Dehn filling that degenerates when the cone angle tends to 2π into a Seifert manifold with hyperbolic base.

We show here a similar phenomenon: a four-dimensional hyperbolic Dehn filling W_t that degenerates as the cone angle tends to 2π into a product $C \times S^1$, where C is a cusped hyperbolic 3–manifold. (The manifold C found here is tessellated into four copies of the ideal right-angled cuboctahedron, and we call it the *cuboctahedral manifold*.) In the following theorem, we think of the time t running backwards from $t = 1$ to $t = 0$, in accordance with Kerckhoff and Storm [13].

Theorem 1.2 *There is an analytic path $\{W_t\}_{t \in (0,1]}$ of complete finite-volume hyperbolic cone four-manifolds with cone angles $< 2\pi$, with some times $1 > t_1 > t_2 > \bar{t} > 0$, such that W_1 is a manifold, and W_{t_1} and $W_{\bar{t}}$ are orbifolds. At the critical times $1, t_1, t_2, 0$ the topology of W_t changes as follows:*

- *at $t = 1$ by hyperbolic Dehn filling 12 three-torus cusps by adding 12 tori;*

Figure 3: The function $\mathrm{Vol}(W_t)$

- at $t = t_1$ by hyperbolic Dehn surgering eight small S^2 with eight small S^1;
- at $t = t_2$ by hyperbolic Dehn surgering four small S^3 with four S^0;
- at $t = 0$, the cone angles tend to 2π and W_t degenerates into $C \times S^1$.

When $t \in (t_1, 1)$, the singular set of W_t is an immersed geodesic surface made of 12 cone tori and 8 cone spheres. When $t \in (0, t_1)$, the singular set is a 2–complex with generic singularities.

The manifolds or orbifolds W_t at the times $t = 1, t_1, \bar{t}$ have Euler characteristic 8, 8 and 5. The volume of W_t is shown in Figure 3. In the degeneration, the holonomy of W_t tends algebraically to the holonomy of C.

The behaviour of W_t when $t \in [t_1, 1]$ is much similar to the one of M_t from Theorem 1.1 when $t \in [0, 1]$, as will be evident from the construction. The cone manifolds W_t are also constructed using the Kerckhoff–Storm deforming polytopes mentioned above.

Structure of the paper

The paper is organised as follows. In Section 2 we recall some well-known facts about (acute-angled) polytopes, Coxeter diagrams and cone manifolds. The main references are the seminal papers of Vinberg [27] and McMullen [18].

In Section 3 we define and study the family of finite-volume polytopes $P_t \subset \mathbb{H}^4$. The quite long section is almost entirely self-contained: many arguments were taken from

the paper of Kerckhoff and Storm [13], which is fundamental for our constructions, and are included for the sake of completeness.

Finally, the deforming cone manifolds W_t, N_t and M_t are constructed in Section 4 by assembling carefully some copies of P_t. Theorems 1.1 and 1.2 are proved there.

Acknowledgements

2 Preliminaries

We introduce in this section some preliminaries on polytopes and cone manifolds, focussing mostly on dimension four.

2.1 Polytopes

We represent the hyperbolic four-space $\mathbb{H}^4$ as the upper sheet of the hyperboloid $\langle v, v \rangle = -1$ in $\mathbb{R}^5$ with respect to the Lorentzian product

$$\langle v, w \rangle = -v_0 w_0 + v_1 w_1 + v_2 w_2 + v_3 w_3 + v_4 w_4.$$

Halfspaces

Every space-like vector v determines a halfspace in $\mathbb{H}^4$ that consists of all $w \in \mathbb{H}^4$ with $\langle v, w \rangle \leq 0$. We are interested in the case where two space-like vectors v and v' determine two halfspaces whose intersection is nonempty and is a proper subset of both halfspaces. There are three possible configurations to consider, easily determined by the number

$$\tag{1} \alpha = \frac{-\langle v, v' \rangle}{\sqrt{\langle v, v \rangle \langle v', v' \rangle}}$$

as follows:

- if $-1 < \alpha < 1$, the boundary hyperplanes of the two halfspaces intersect with a dihedral angle θ such that $\cos \theta = \alpha$;
- if $\alpha = 1$, the boundary hyperplanes are asymptotically parallel;
- if $\alpha > 1$, the boundary hyperplanes are ultraparallel, and their distance d is such that $\cosh d = \alpha$.

Finite polytopes

We define as usual a (*finite convex*) *polytope* to be the intersection P of finitely many halfspaces in $\mathbb{H}^4$, with the additional hypothesis that $\mathrm{int}(P) \neq \varnothing$. The boundary ∂P is naturally stratified into *vertices*, *edges*, *faces* and *walls* (also called *facets*).

If the closure $\overline{P}$ of P in the compactification $\overline{\mathbb{H}^4}$ intersects $\partial \mathbb{H}^4$ in finitely many (possibly zero) points, the volume of P is finite; otherwise it is infinite. These points in $\partial \mathbb{H}^4$ are called *ideal vertices*.

Volume

To compute the volume of a finite-volume, even-dimensional polytope P there is a formula due to Poincaré (see [1, page 120]). Denoting by L_S the spherical link of the stratum S and by α_F the dihedral angle at the (two-dimensional) face F, in dimension four the formula is

$$\mathrm{Vol}(P) = \frac{4\pi^2}{3}\left(1 - \frac{1}{2}N + \frac{1}{2\pi}\sum_{F \text{ face}} \alpha_F - \frac{1}{4\pi}\sum_{E \text{ edge}} \mathrm{Area}(L_E) + \frac{1}{2\pi^2}\sum_{V \text{ vertex}} \mathrm{Vol}(L_V)\right),$$

where N is the number of walls.

In any dimension, there is also the well-known Schläfli formula (also on [1, page 122]) that expresses the variation of the volume of a deforming polytope P (whose combinatorics stays constant) in terms of the area of the faces and of the variation of the dihedral angles. In dimension four, it is

$$d\,\mathrm{Vol}(P) = -\frac{1}{3}\sum_{F \text{ face}} \mathrm{Area}(F)\, d\alpha_F.$$

To apply that formula, recall that the area of a hyperbolic k–gon F with inner angles $\alpha_1, \ldots, \alpha_k$ is

$$\mathrm{Area}(F) = (k-2)\pi - \sum_{i=1}^{k} \alpha_i.$$

Topology

Let X be a compact metric space. Recall that the Hausdorff distance defines a topology on the closed subsets of X which depends only on the topology of X.

Every polytope and more generally every closed subset $C \subset \mathbb{H}^n$ has a compactification $\overline{C} \subset \overline{\mathbb{H}^n}$. We endow the family of all closed subsets $C \subset \mathbb{H}^n$ with the Hausdorff distance topology of their compactifications in $\overline{\mathbb{H}^n}$ (here $\overline{\mathbb{H}^n}$ is equipped with any compatible metric). Note that the volume function on this family is not continuous.

This topology will be used tacitly throughout all the paper. The situation that is relevant here is when a family of polytopes is defined as the intersection of some moving halfspaces determined by some space-like vectors $v_1, \ldots, v_m$. If the vectors $v_1, \ldots, v_m$ move continuously, the polytope deforms continuously.

2.2 Acute-angled polytopes

The theory of acute-angled hyperbolic polytopes is beautifully introduced in a paper of Vinberg [27] and we briefly recall some of the facts described in that paper. We stick to dimension four for simplicity, although everything applies to any dimension.

Gram matrix

Let $P \subset \mathbb{H}^4$ be a polytope, defined as the intersection of the halfspaces dual to some unit space-like vectors $v_1, \ldots, v_m$. We calculate α_{ij} from v_i and v_j using (1) for any i and j. The $m \times m$ matrix $-\alpha_{ij}$ is the *Gram matrix* of P; see [27].

We say that P is *acute-angled* if $\alpha_{ij} \geq 0$ for all $i \neq j$. Acute-angled polytopes have many nice properties. In this section, we will always suppose that P is acute-angled.

Remark 2.1 By a theorem of Andreev [2], a generic polytope P is acute-angled if and only if all its dihedral angles are $\leq \frac{\pi}{2}$, and this explains the terminology.

Generalised Coxeter diagrams

The Gram matrix of an acute-angled polytope P is nicely encoded via the *generalised Coxeter diagram* D of P, which is constructed as follows: every vertex of D represents a vector v_i and every edge between two distinct vertices v_i and v_j has a label that depends on $\alpha_{ij} \geq 0$ as follows:

- If $\alpha_{ij} > 1$, the edge is dashed (and sometimes labelled with the number $d > 0$ such that $\cosh d = \alpha_{ij}$, but we will not do that).
- If $\alpha_{ij} = 1$, the edge is thickened.
- If $0 \leq \alpha_{ij} < 1$, the edge is labelled with the angle $\frac{\pi}{2} \geq \theta > 0$ such that $\cos \theta = \alpha_{ij}$.

To simplify the picture, the edges labelled with an angle $\frac{\pi}{2}$ are not drawn, and in those with $\frac{\pi}{3}$ the label is omitted.

Strata

The following facts are proved in [27, Section 3]. Every acute-angled polytope P is *simple*, that is, each stratum S of P of codimension k is contained in exactly k walls.

All the strata of P may be easily determined from D as follows:

- The vertices v_i represent the walls of P.

- The pairs of vertices connected by an edge labelled with some angle θ represent the faces of P; the angle θ is the dihedral angle of that face.

- More generally, the strata S of codimension k correspond to the k–tuples of vertices of D whose subdiagram represents a $(k-1)$–dimensional spherical simplex L_S; the spherical simplex L_S is geometrically the link of S.

In particular, the set of vectors $v_1, \ldots, v_m$ defining P is minimal (no proper subset defines P), and k walls in P intersect if and only if the hyperplanes containing them do. These nice facts are not true in general for non-acute-angled polytopes.

Diagrams of the strata

Every stratum S of an acute-angled polytope P is also acute-angled, and one can deduce a Coxeter diagram D_S for S from the diagram D of P. We explain how this works in the easier case when S is a wall; the procedure can then be applied iteratively.

The diagram D_S is formed by all the vertices of D that represent walls that are incident to S; that is, D_S is constructed from D by removing the vertex v_i corresponding to S and all the vertices v_j that are connected to v_i by either a dashed or a thickened edge.

The resulting diagram D_S is *not* yet a generalised Coxeter diagram for S, because the value of α from formula (1) needs to be recomputed for every edge. To do so we must substitute each space-like vector v_j with its projection $P(v_j)$ in the time-like hyperplane $v_i^\perp$ containing S, using the formula

$$P(v_j) = v_j - \frac{\langle v_j, v_i \rangle}{\langle v_i, v_i \rangle} v_i.$$

The new $\alpha \geq 0$ is computed using the projections $P(v_j)$ and is equal to or bigger than the original one (in particular, S is still acute-angled).

Ideal vertices

The ideal vertices v of P are also detected in a similar fashion: they correspond to the subdiagrams of D that represent some compact 3–dimensional Euclidean acute-angled polyhedron Q, which is in fact the link of v. The polyhedron Q must be a product of simplexes, so the subdiagram is a disjoint union of diagrams representing Euclidean

simplexes. (In all dimensions, every acute-angled spherical polytope without antipodal points is a simplex, and every acute-angled compact Euclidean polytope is a product of Euclidean simplexes.)

There is a combinatorial criterion that one can use to check from D whether P is compact and/or has finite volume; see [27, Proposition 4.2]. We suppose that P contains at least one (finite or ideal) vertex.

Theorem 2.2 *The polytope P is compact (resp. has finite volume) if and only if each of its edges joins exactly two finite (resp. finite or ideal) vertices.*

This condition is designed to exclude the presence of hyperideal vertices; see [27]. In this paper we will only deal with finite-volume polytopes.

Coxeter polytopes

If all the dihedral angles of P are of type $\frac{\pi}{n}$ for some $n \geq 2$, then P is a *Coxeter polytope*. In this case the group $\Gamma < \mathrm{Isom}(\mathbb{H}^4)$ generated by the reflections along its walls is discrete and has P as a fundamental domain, so that $P = \mathbb{H}^4/\Gamma$ may be interpreted as an orbifold.

Recall that the orbifold Euler characteristic of a Coxeter polytope P is given by the formula

$$\chi(P) = \sum_{s} \frac{(-1)^{\dim(s)}}{|\mathrm{Stab}(s)|},$$

where the sum is over all the strata s of the polytope (ideal vertices are excluded) and $\mathrm{Stab}(s)$ is the stabiliser of a stratum inside the Coxeter reflection group of P.

2.3 Cone manifolds

Constant-curvature cone manifolds (and more generally (X, G)–cone manifolds) were defined by Thurston [26] inductively on the dimension as follows: a cone 1–manifold is an ordinary Riemannian 1–manifold, and a hyperbolic (or Euclidean, spherical) cone n–manifold is locally a hyperbolic (or Euclidean, spherical) cone over a compact connected spherical cone $(n-1)$–manifold.

Every point $p \in M$ in a hyperbolic (or Euclidean, spherical) cone n–manifold M is locally a cone over a compact spherical cone $(n-1)$–manifold $S_p(M)$, called the *unit tangent space* to M at p. If $S_p(M)$ is isometric to S^{n-1}, the point is *regular*, and it

is *singular* otherwise. The singular points form the *singular set* $\Sigma \subset M$. McMullen defined a natural stratification on Σ that we now recall; see [18] for more details (and proofs).

Let EA denote the Euclidean cone over a spherical cone manifold A. The *join* $A * B$ of two spherical cone manifolds A and B is defined as

$$A * B = S_{(0,0)}(EA \times EB).$$

In particular we have $S^m * S^n \cong S^{m+n+1}$. We set $S^{-1} = \varnothing$. It is proved in [18, Theorem 5.1] that every compact spherical cone manifold N decomposes uniquely as a join

$$N \cong S^{k-1} * B$$

for some $k \geq 0$ and some *prime* B, that is, a B that does not decompose further as $B = S^0 * C$. Let now M be a hyperbolic (or Euclidean, spherical) cone n–manifold. We define

$$M[k] = \{p \in M \mid S_p(M) \cong S^{k-1} * B \text{ with } B \text{ prime}\}.$$

A k–*stratum* of M is a connected component of $M[k]$. It is a totally geodesic k–dimensional hyperbolic (or Euclidean, spherical) manifold. Points lying in the same k–stratum have isometric unit tangent spaces.

The regular points form the open dense set $M[n]$, and $M[n-1]$ is empty. The singular set $\Sigma = \bigcup_{k<n} M[k]$ has codimension at least two. If M is complete (as will always be the case in this paper) then M is the metric completion of $M[n] = M \setminus \Sigma$.

We denote by C_θ the Riemannian circle of length θ. The unit tangent space of a point $p \in M[n-2]$ is a join $S^{n-3} * C_\theta$ for some number $\theta \neq 2\pi$ that depends only on the stratum containing p, called the *cone angle* of that stratum.

We list some examples of constant-curvature cone manifolds.

Cone surfaces

A hyperbolic (or Euclidean, spherical) cone surface S has some isolated singularities, each with a cone angle $\theta \neq 2\pi$. Simple examples may be constructed by doubling polygons along their boundaries.

If we double a spherical bigon with inner angles $\frac{\theta}{2}$, we get a cone sphere with two singular points of angle θ, which is isometric to the join $S^0 * C_\theta$. If we double a
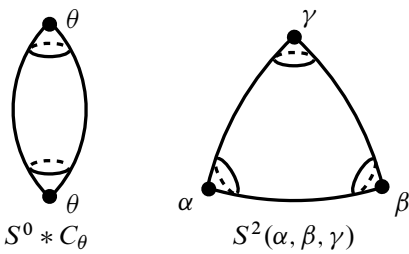
Figure 4: The elliptic cone surfaces $S^0 * C_\theta$ and $S^2(\alpha, \beta, \gamma)$

spherical triangle with inner angles $\frac{\alpha}{2}, \frac{\beta}{2}, \frac{\gamma}{2}$, we get a cone sphere with three singular points of cone angles α, β, γ. This is a prime spherical cone surface and we denote it by $S^2(\alpha, \beta, \gamma)$. See Figure 4.

By Gauss–Bonnet, every compact connected orientable spherical cone surface with cone angles $< 2\pi$ is a sphere with some singular points (possibly none).

Cone three-manifolds

On a hyperbolic (or Euclidean, spherical) cone 3–manifold M the singular set $\Sigma = M[0] \cup M[1]$ has dimension ≤ 1. Each 1–stratum has some cone angle θ, while the unit tangent space at every point $p \in M[0]$ is some prime spherical cone surface. For instance, it may be $S^2(\alpha, \beta, \gamma)$.

Some spherical cone 3–manifolds are shown in Figure 5. The join $S^1 * C_\theta$ is S^3 with an unknotted closed geodesic of length 2π and of cone angle θ. The join $S^0 * S^2(\alpha, \beta, \gamma)$ is S^3 with singular set $\ominus$ and cone angles α, β, γ. If we double a spherical tetrahedron with dihedral angles $\frac{\alpha}{2}, \ldots, \frac{\zeta}{2}$, we get S^3 with singular set the 1–skeleton $\oslash$ of a tetrahedron and cone angles $\alpha, \ldots, \zeta$; this is a prime spherical cone 3–manifold.

A spherical cone 3–manifold that is crucial in this paper is the join $C_\theta * C_\varphi$ with $\theta, \varphi \neq 2\pi$ shown in Figure 5, right. This is S^3 with singular set the Hopf link: one
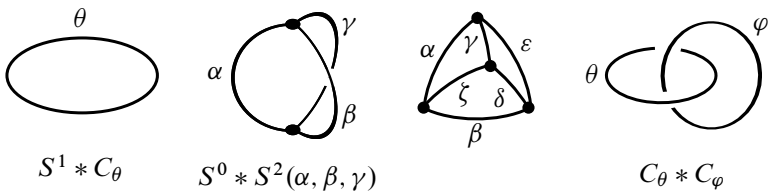

Figure 5: Some simple spherical cone 3–manifolds. In all cases the underlying manifold is S^3.
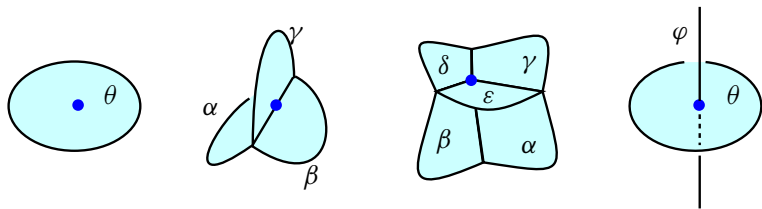
Figure 6: Singular points in a cone four-manifold with unit tangent space as in Figure 5. In the right picture we have two discs intersecting transversely in a point, with cone angles θ and φ. In all cases the singularity lies locally in a topological four-ball; a cone manifold with this kind of singularity is topologically a manifold.

component of the Hopf link has length θ and cone angle φ, while the other has length φ and cone angle θ. This is a prime spherical cone 3–manifold (although it decomposes nontrivially as a join).

If we assume that all cone angles are $< 2\pi$, then every orientable hyperbolic (or Euclidean, spherical) cone 3–manifold is supported on a manifold.

Cone four-manifolds

On a hyperbolic (or Euclidean, spherical) cone 4–manifold M, the singular set $\Sigma = M[0] \cup M[1] \cup M[2]$ has dimension ≤ 2. Each 2–stratum has some cone angle θ. In each 1–stratum the unit tangent space of a point is $S^0 * B$ for some prime spherical cone surface B. At each 0–stratum, the unit tangent space is a prime spherical cone 3–manifold.

Figure 6 shows the types of singularities in a cone 4–manifold that we will encounter in this paper; they are obtained by coning the spherical cone manifolds shown in Figure 5, and are in some sense the simplest kind of singularities that may occur in dimension four. A hyperbolic cone four-manifold with these types of singularities is topologically a manifold.

Example 2.3 If we pick a compact acute-angled (hence simple) polytope $P \subset \mathbb{H}^4$ and double it along its boundary, we get a hyperbolic cone manifold with underlying space S^4 and singularities of the first three kinds shown in Figure 6. A 2–complex Σ with these generic local singularities is sometimes called a *foam*.

If $M[1] = \varnothing$ and the unit tangent space at every point in $M[0]$ is isometric to $C_\theta * C_\varphi$ (that is, if the only singularities in M are like the first and the last one in Figure 6),

we say that Σ is an *immersed geodesic cone surface*. In this case we may see Σ as the image of a geodesic immersion $\tilde{\Sigma} \looparrowright M$ of a hyperbolic cone surface $\tilde{\Sigma}$ obtained by resolving the double points of Σ lying in $M[0]$. Every point p in $M[0]$ with unit tangent space $C_\theta * C_\varphi$ is the image of two singular points in $\tilde{\Sigma}$ with cone angles θ and φ. The hyperbolic cone four-manifolds that arise in Theorem 1.1 are of this kind.

3   The polytopes

We now introduce a family of finite-volume polytopes $P_t \subset \mathbb{H}^4$ that depend on a parameter $t \in (0, 1]$, obtained by deforming the *ideal right-angled 24–cell P_1*. The family is constructed by truncating the infinite-volume polytopes $\mathcal{F}_t$ built by Kerckhoff and Storm [13] with two additional hyperplanes. We try to follow [13] as much as we can, reproducing all the notation used there. As in [13], we will think of this deformation running backwards from $t = 1$, starting with the ideal 24–cell P_1 and eventually degenerating to a three-dimensional polyhedron (an ideal cuboctahedron) when $t \to 0$.

In Section 4 we will use P_t to construct the deforming hyperbolic cone manifolds M_t and W_t needed to prove Theorems 1.1 and 1.2. We warn the reader that the time parameter t used for P_t and W_t differ from that employed to define M_t by a linear rescaling: the manifold M_t of Theorem 1.1 will be constructed by employing P_t within the segment
$$t \in \left[\sqrt{3/5}, 1\right].$$
The times $t < \sqrt{3/5}$ will not be used to prove Theorem 1.1, but only to prove Theorem 1.2. The reader interested only in Theorem 1.1 may thus ignore our discussion on P_t when $t < \sqrt{3/5}$.

There are in fact two very important times in the deformation P_t where the polytope changes its combinatorics. These are
$$t_2 = \sqrt{1/2}, \quad t_1 = \sqrt{3/5}.$$

The combinatorics also changes at the initial time $t = 1$ and at the final time $t = 0$ where P_t degenerates to a three-dimensional polyhedron. We will sometimes call 0, t_2, t_1 and 1 the *critical times* of the family P_t.

Many of the results presented in this section were first proved in [13] and we include them here only for the sake of completeness.

$$0^+ = (\sqrt{2}, 1, 1, 1, 1/t), \qquad 0^- = (\sqrt{2}, 1, 1, 1, -t),$$
$$1^+ = (\sqrt{2}, 1, -1, 1, -1/t), \qquad 1^- = (\sqrt{2}, 1, -1, 1, t),$$
$$2^+ = (\sqrt{2}, 1, -1, -1, 1/t), \qquad 2^- = (\sqrt{2}, 1, -1, -1, -t),$$
$$3^+ = (\sqrt{2}, 1, 1, -1, -1/t), \qquad 3^- = (\sqrt{2}, 1, 1, -1, t),$$
$$4^+ = (\sqrt{2}, -1, 1, -1, 1/t), \qquad 4^- = (\sqrt{2}, -1, 1, -1, -t),$$
$$5^+ = (\sqrt{2}, -1, 1, 1, -1/t), \qquad 5^- = (\sqrt{2}, -1, 1, 1, t),$$
$$6^+ = (\sqrt{2}, -1, -1, 1, 1/t), \qquad 6^- = (\sqrt{2}, -1, -1, 1, -t),$$
$$7^+ = (\sqrt{2}, -1, -1, -1, -1/t), \quad 7^- = (\sqrt{2}, -1, -1, -1, t),$$
$$A = (1, \sqrt{2}, 0, 0, 0), \qquad B = (1, 0, \sqrt{2}, 0, 0),$$
$$C = (1, 0, 0, \sqrt{2}, 0), \qquad D = (1, 0, 0, -\sqrt{2}, 0),$$
$$E = (1, 0, -\sqrt{2}, 0, 0), \qquad F = (1, -\sqrt{2}, 0, 0, 0),$$
$$G = (1, 0, 0, 0, -\sqrt{2}t), \qquad H = (1, 0, 0, 0, \sqrt{2}t).$$

Table 1: The halfspaces that define P_t are the duals of these space-like vectors: we denote vectors and halfspaces by the same letters. These vectors are indeed space-like for all $t \in (0, 1]$, except G and H that are space-like only for $t \in (t_2, 1]$.

3.1 The family P_t

We define

$$t_2 = \sqrt{1/2}$$

and we consider the 24 halfspaces $0^+, 0^-, \ldots, G, H$ listed in Table 1, which depend on some parameter t. The parameter t varies in $(0, 1]$ for $0^+, 0^-, \ldots, E, F$ and only in $(t_2, 1]$ for G and H. The reader may check that for these values the vectors listed in the table are indeed space-like and hence determine some halfspaces in $\mathbb{H}^4$.

For every $t \in (0, 1]$ we define P_t as the intersection of all the halfspaces in the table that are present at the time t. That is:

Definition 3.1 Let P_t be the intersection of the 24 halfspaces $0^+, 0^-, \ldots, G, H$ when $t \in (t_2, 1]$, and of the 22 halfspaces $0^+, 0^-, \ldots, E, F$ when $t \in (0, t_2]$.

Proposition 3.2 *The set P_t is a polytope for all $t \in (0, 1]$ that deforms continuously in $t \in (0, 1]$.*

Proof To prove that P_t is a polytope we only need to check that its interior is nonempty. The set P_t contains a small ball centred at the point $(1, 0, 0, 0, 0)$, because the first entry of each vector in Table 1 is positive for every $t \in (0, 1]$.

The deformation is clearly continuous, also at the singular time $t = t_2$ because the halfspaces $\boldsymbol{G}$ and $\boldsymbol{H}$ tend to the full $\mathbb{H}^4$ as $t \to t_2$ (the space-like vertices defining them tend to light-like vertices). $\qquad \square$

The walls

The walls of P_t are easily determined. We prove that the set of halfspaces that defines P_t is minimal.

Proposition 3.3 *The boundary of each halfspace $\boldsymbol{0}^+, \boldsymbol{0}^- \ldots, \boldsymbol{G}, \boldsymbol{H}$ intersects P_t in a wall for all $t \in (0, 1]$ for $\boldsymbol{0}^+, \boldsymbol{0}^-, \ldots, \boldsymbol{E}, \boldsymbol{F}$ and for all $t \in (t_2, 1]$ for $\boldsymbol{G}$ and $\boldsymbol{H}$.*

Proof The point $(\sqrt{2}, \frac{2}{3}, \frac{2}{3}, \frac{2}{3}, 0)$ belongs to the boundaries of both $\boldsymbol{0}^+$ and $\boldsymbol{0}^-$ and lies in the interior of all the other halfspaces: this proves the assertion for $\boldsymbol{0}^+$ and $\boldsymbol{0}^-$. By changing the signs of the $\frac{2}{3}$ entries we obtain the same for the other positive and negative faces.

The point $(\sqrt{2}, 1, 0, 0, 0)$ belongs to the boundary of $\boldsymbol{A}$ and lies in the interior of the other halfspaces. Similar points work for $\boldsymbol{B}, \ldots, \boldsymbol{F}$. The points $(\sqrt{2}t, 0, 0, 0, \mp 1)$ work for $\boldsymbol{G}$ and $\boldsymbol{H}$ when $t > t_2$. $\qquad \square$

The polytope P_t has 24 walls if $t \in (t_2, 1]$ and 22 walls if $t \in (0, t_2]$. We denote the walls of P_t by the same symbols $\boldsymbol{0}^+, \boldsymbol{0}^-, \ldots, \boldsymbol{G}, \boldsymbol{H}$ of the corresponding halfspaces.

Remark 3.4 Kerckhoff and Storm define for every $t \in (0, 1]$ a bigger polytope $\mathcal{F}_t$ as the intersection of the 22 halfspaces $\boldsymbol{0}^+, \boldsymbol{0}^-, \ldots, \boldsymbol{E}, \boldsymbol{F}$. The polytope $\mathcal{F}_t$ coincides with P_t for $t \in (0, t_2]$; it has infinite volume for $t \in (t_2, 1]$ and finite volume for $t \in (0, t_2]$. We will soon check that P_t has finite volume for all $t \in (0, 1]$.

The right-angled ideal regular 24–cell

As remarked in [13, Section 3], the polytope P_1 is the regular right-angled ideal 24–cell. The adjacencies between the walls $\boldsymbol{0}^+, \boldsymbol{0}^-, \ldots, \boldsymbol{G}, \boldsymbol{H}$ of P_1 are nicely codified in [13, Figure 3.1].

The 24 walls of P_1 are subdivided into three octets: the *positive*, the *negative* and the *letter* walls; see Table 1. Two walls of the same octet are never adjacent; this is the standard three-colouring of the 24–cell that was used in [15] to construct many hyperbolic four-manifolds.

The right-angled ideal cuboctahedron

What happens as $t \to 0$? When $t = 0$, the negative $\mathbf{0}^-, \dots, \mathbf{7}^-$ and letter halfspaces $A, \dots F$ are still defined. As $t \to 0$, every positive halfspace converges to $(0, 0, 0, 0, \pm 1)$, so they are also still defined (we keep identifying space-like vectors and halfspaces). We may still set P_0 to be the intersection of the halfspaces $\mathbf{0}^+, \mathbf{0}^-, \dots, E, F$. As $t \to 0$, the polytope P_t converges to P_0.

Among the halfspaces defining P_0 we find both $(0, 0, 0, 0, 1)$ and $(0, 0, 0, 0, -1)$, hence P_0 is contained in the hyperbolic hyperplane $\{x_4 = 0\}$ isometric to $\mathbb{H}^3$. Therefore, P_0 is some lower-dimensional object. It is proved in [13] that $P_0 \subset \mathbb{H}^3$ is a three-dimensional ideal polyhedron, and more precisely a right-angled ideal cuboctahedron; see also Proposition 3.19 below. It has 14 faces, defined by the intersections of the 14 walls $\mathbf{0}^-, \mathbf{1}^-, \dots, E, F$ with $\mathbb{H}^3$.

Summing up, the family P_t is a continuous deformation of polytopes that starts with the ideal regular right-angled 24–cell P_1 and eventually degenerates to the ideal right-angled cuboctahedron P_0.

3.2 Symmetries

In the next sections, we will determine the combinatorics of the polytope P_t for all times $t \in (0, 1)$. Luckily, each P_t has a big group of symmetries that will simplify our arguments significantly.

Consider the halfspaces determined by the space-like vectors

$$L = (0, -1, 1, 0, 0), \quad M = (0, 0, -1, 1, 0), \quad N = (0, 0, -1, -1, 0).$$

We denote by the same symbols the halfspaces and the reflections in the corresponding hyperplanes. These reflections act as follows:

$$L \colon (x_0, x_1, x_2, x_3, x_4) \mapsto (x_0, x_2, x_1, x_3, x_4),$$
$$M \colon (x_0, x_1, x_2, x_3, x_4) \mapsto (x_0, x_1, x_3, x_2, x_4),$$
$$N \colon (x_0, x_1, x_2, x_3, x_4) \mapsto (x_0, x_1, -x_3, -x_2, x_4).$$

Consider the group

$$H = \langle L, M, N \rangle.$$

The group H is isomorphic to the symmetric group $\mathcal{S}_4$ (note that $(MN)^2 = (LN)^3 = (LM)^3 = 1$). Moreover, in [13, Section 4] it is shown that H is the group of symmetries of the 24–cell P_1 that preserve

- the positive/negative/letter colours of the walls;
- the even/odd parity of the numbered walls;
- the walls G and H (individually).

The group H acts on the set of four positive (or negative) even (or odd) walls as its full permutation group. Up to the action of H, the 24 walls $\{0^+, 0^-, \ldots, G, H\}$ reduce to the set

$$\{0^+, 0^-, 3^+, 3^-, A, G, H\}.$$

Now, consider the order-two rotation

$$R: (x_0, x_1, x_2, x_3, x_4) \mapsto (x_0, x_1, x_2, -x_3, -x_4).$$

This rotation is called the *roll symmetry* in [13]. It still preserves P_1 and the positive/negative/letter colours of the walls, but it changes the parity of any numbered wall and it exchanges the walls G and H. Kerckhoff and Storm prove that the extension

$$K = \langle L, M, N, R \rangle$$

has order 48 and consists precisely of the symmetries of P_1 that preserve the colours of the walls and the pair $\{G, H\}$. Up to the action of K the set of walls is further reduced to

$$\{3^+, 0^-, A, G\}.$$

It is immediate to note that K is also a group of symmetries of P_t for every t (in fact, it will be clear later that K is the full group of symmetries of P_t when $t < 1$). Up to symmetries the polytope P_t has only four types of walls.

3.3 The quotient polytope Q_t

As in [13], we can quotient P_t by the group H of symmetries, and obtain an interesting smaller polytope Q_t with a smaller number of walls. (If we quotient P_t by K we do not get a polytope!)

The quotient polytope Q_t may be identified with the intersection of P_t with the halfspaces $\boldsymbol{L}$, $\boldsymbol{M}$ and $\boldsymbol{N}$. The walls of Q_t are

$$\{\boldsymbol{0^+}, \boldsymbol{0^-}, \boldsymbol{3^+}, \boldsymbol{3^-}, \boldsymbol{A}, \boldsymbol{G}, \boldsymbol{H}, \boldsymbol{L}, \boldsymbol{M}, \boldsymbol{N}\}$$

when $t \in (t_2, 1]$, and the same list with $\boldsymbol{G}$ and $\boldsymbol{H}$ removed when $t \in (0, t_2]$. The roll symmetry R is a symmetry of Q_t that permutes each pair

$$\{\boldsymbol{0^+}, \boldsymbol{3^+}\}, \quad \{\boldsymbol{0^-}, \boldsymbol{3^-}\}, \quad \{\boldsymbol{G}, \boldsymbol{H}\}, \quad \{\boldsymbol{M}, \boldsymbol{N}\}$$

and preserves the walls $\boldsymbol{L}$ and $\boldsymbol{A}$. We introduce another critical time,

$$t_1 = \sqrt{3/5}.$$

Note that $0 < t_2 < t_1 < 1$. We now show that the quotient polytope Q_t is acute-angled for all $t \in (0, 1]$ and may be fully described by some reasonable Coxeter diagrams, whose combinatorics changes at the critical times 1, t_1 and t_2.

Proposition 3.5 *The polytope Q_t is acute-angled for all $t \in (0, 1]$. Its generalised Coxeter diagram D_t is shown in [Figure 7](#) for all $t \in (0, 1]$. The dihedral angles $\frac{\theta}{2}$ and φ are such that*

$$\cos \theta = \frac{3t^2 - 1}{1 + t^2}, \quad \cos \varphi = \frac{\sqrt{2}(1 - t^2)}{\sqrt{(2t^2 - 1)(t^2 + 1)}}.$$

The dihedral angles $\frac{\theta}{2}$ and φ are defined for $t \in (0, 1)$ and $t \in (t_1, 1]$, respectively. They both vary strictly monotonically in t. We have

$$\lim_{t \to 1} \tfrac{\theta}{2}(t) = 0, \quad \tfrac{\theta}{2}(t_1) = \tfrac{\pi}{6}, \quad \lim_{t \to 0} \tfrac{\theta}{2}(t) = \tfrac{\pi}{2}, \quad \varphi(1) = \tfrac{\pi}{2}, \quad \lim_{t \to t_1} \varphi(t) = 0.$$

We plot the functions $\theta(t)$ and $\varphi(t)$ in [Figure 8](#).

Proof We use the formula [(1)](#) for every pair of walls in the set

$$(2) \qquad \{\boldsymbol{0^+}, \boldsymbol{0^-}, \boldsymbol{3^+}, \boldsymbol{3^-}, \boldsymbol{A}, \boldsymbol{G}, \boldsymbol{H}, \boldsymbol{L}, \boldsymbol{M}, \boldsymbol{N}\}.$$

We use the roll symmetry R to reduce the number of pairs to be investigated. A simple inspection shows that we get $\alpha \geq 0$ for every pair and at every time $t \in (0, 1]$. More precisely, for most pairs we get $\alpha > 1$, $\alpha = 1$, $\alpha = \frac{1}{2}$ or $\alpha = 0$ for all $t \in (0, 1]$, except (up to the roll symmetry) for the following:

(1) With the pair $\{\boldsymbol{0^+}, \boldsymbol{N}\}$ we get

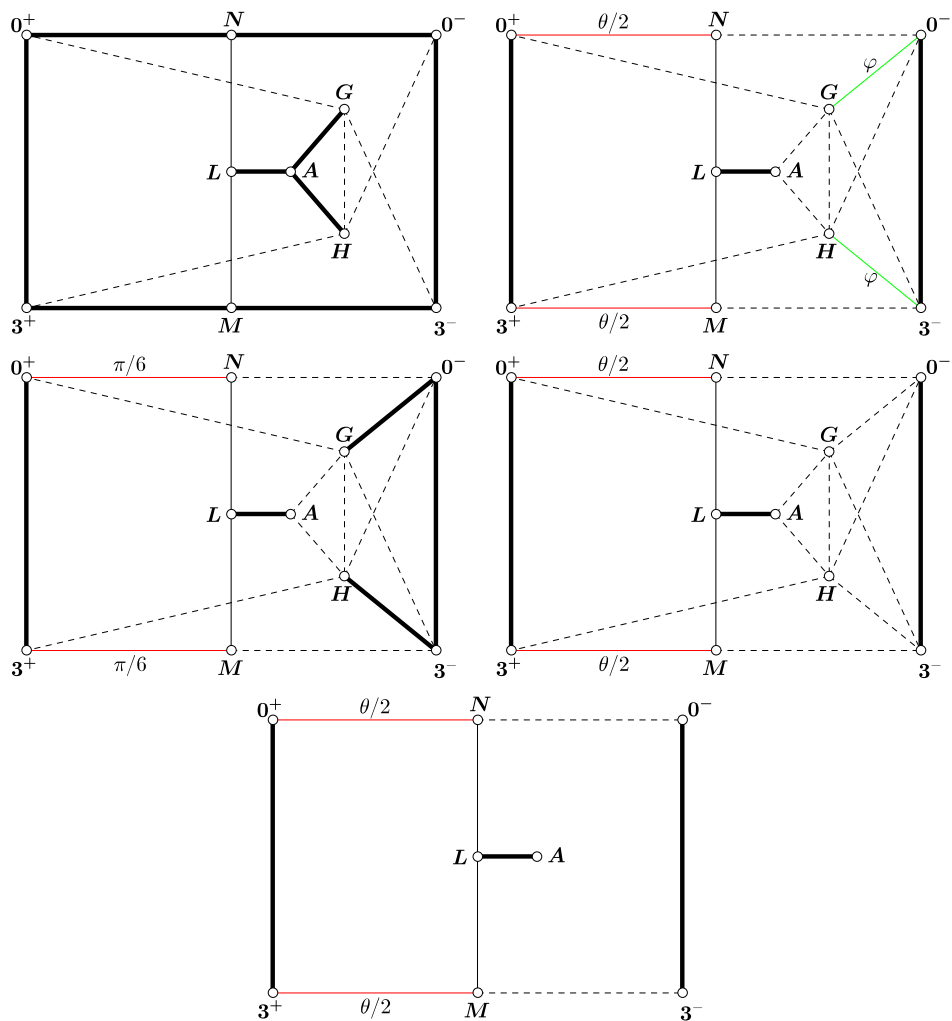$$\alpha = \frac{\sqrt{2}t}{\sqrt{1 + t^2}} > 0.$$

Figure 7: The generalised Coxeter diagram D_t of Q_t when $t = 1$, $t \in (t_1, 1)$, $t = t_1$, $t \in (t_2, t_1)$ and $t \in (0, t_2]$, respectively. The green and red edges indicate the faces with varying dihedral angle φ and $\frac{\theta}{2}$.

(2) With the pair $\{0^-, G\}$ we get

$$\alpha = \frac{\sqrt{2}(1 - t^2)}{\sqrt{(2t^2 - 1)(t^2 + 1)}} \geq 0;$$

recall that G exists only for $t > t_2 = \sqrt{1/2}$.

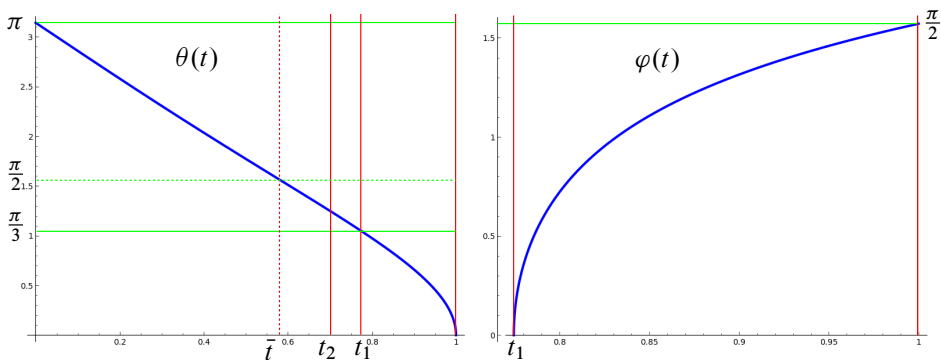(3) With the pairs $\{0^-, N\}$ and $\{A, G\}$ we get $\alpha = 1$ at $t = 1$ and $\alpha > 1$ for $t < 1$.

Figure 8: The functions θ and φ. We note the critical times t_2 and t_1. At the noncritical time $\bar{t} = \sqrt{1/3}$ we get $\theta = \frac{\pi}{2}$.

Therefore Q_t is acute-angled for all $t \in (0, 1]$. Concerning the Coxeter diagrams, we note that:

(1) With the pair $\{\mathbf{0^+}, \mathbf{N}\}$, we get $\alpha = 1$ at $t = 1$ and $\alpha < 1$ for all $t < 1$. Therefore when $t < 1$ the walls intersect with dihedral angle $\frac{\theta}{2}$ such that $\cos \frac{\theta}{2} = \alpha$, that is,

$$\cos \theta = 2 \cos^2 \frac{\theta}{2} - 1 = 2\alpha^2 - 1 = 2\frac{2t^2}{1 + t^2} - 1 = \frac{3t^2 - 1}{1 + t^2}.$$

In particular when $t = t_1$ we get $\cos \theta = \frac{1}{2}$ and hence $\frac{\theta}{2} = \frac{\pi}{6}$. By calculating the derivative one sees that θ varies strictly monotonically in t.

(2) With the pair $\{\mathbf{0^-}, \mathbf{G}\}$, we get $\alpha = 0$ at $t = 1$. When $t \in (t_1, 1)$ we get $0 < \alpha < 1$ and the halfspaces intersect with dihedral angle φ such that $\cos \varphi = \alpha$. By calculating the derivative we see that φ varies monotonically in t. When $t = t_1$ we get $\alpha = 1$ and when $t < t_1$ we get $\alpha > 1$. □

The roll symmetry R acts on the Coxeter diagram of Q_t as a reflection with horizontal axis. The polytopes Q_t are remarkable because they are acute-angled and have only few nonright dihedral angles for every t.

Coxeter polytopes

Recall that a Coxeter polytope is a polytope whose dihedral angles divide π. As noted in [13], the polytope Q_t is Coxeter at the times

$$1, \quad t_1 = \sqrt{3/5}, \quad \frac{\cos \frac{\pi}{5}}{\sqrt{1 + \sin^2 \pi/5}}, \quad \sqrt{1/3}, \quad \sqrt{1/7}.$$

For these times, the dihedral angle $\frac{\theta}{2}$ is, respectively,

$$0, \quad \frac{\pi}{6}, \quad \frac{\pi}{5}, \quad \frac{\pi}{4}, \quad \frac{\pi}{3}.$$

The dihedral angle φ is $\frac{\pi}{2}$ and 0 in the first two cases. We get five Coxeter polytopes overall in the family Q_t. Using Vinberg's criterion, in [13] it is proved that they are all arithmetic, except the one with $\frac{\theta}{2} = \frac{\pi}{5}$.

The walls

We now describe the 3–dimensional walls of Q_t. Up to the roll symmetry R, there are only six walls to analyse in Q_t, namely

$$\mathbf{0^-}, \quad \mathbf{3^+}, \quad A, \quad G, \quad L, \quad M.$$

Each such wall is an acute-angled polyhedron, because Q_t is acute-angled. We are only interested in the first four, $\mathbf{0^-}, \mathbf{3^+}, A, G$, which are quotients of some walls in P_t; understanding these will be enough to determine the combinatorics of all the walls in the original polytope P_t. We ignore the case $t = 1$ for simplicity: we already know that P_1 is the ideal regular 24–cell.

Lemma 3.6 *The generalised Coxeter diagrams of the acute-angled polyhedra A, G, $\mathbf{0^-}$ and $\mathbf{3^+}$ are shown in Figure 9 for all $t \in (0, 1)$. The (yellow) dihedral angle $\frac{\psi}{2}$ of $\mathbf{3^+}$ is defined for $t \in (0, t_1]$ and is such that*

$$\cos \psi = \frac{\cos \theta}{1 - \cos \theta} = \frac{1 - 3t^2}{2(t^2 - 1)}.$$

In particular, the angle $\frac{\psi}{2}$ varies strictly monotonically in t. Its extremal values are

$$\lim_{t \to t_1} \frac{\psi}{2}(t) = 0, \quad \lim_{t \to 0} \frac{\psi}{2}(t) = \frac{\pi}{3}.$$

Proof For every $W \in \{A, G, \mathbf{0^-}, \mathbf{3^+}\}$ and every time t, we construct the Coxeter diagram $D_{W,t}$ of W at time t following the instructions of Section 2.2.

The diagram $D_{W,t}$ is built from D_t by removing W and all the vertices that are connected to W by either a dashed or a thickened edge. We need then to recompute α from formula (1) for every pair of vectors. To do so we must substitute each space-like vector

$$v \in \{\mathbf{0^+}, \mathbf{0^-}, \mathbf{3^+}, \mathbf{3^-}, A, G, H, L, M, N\}$$
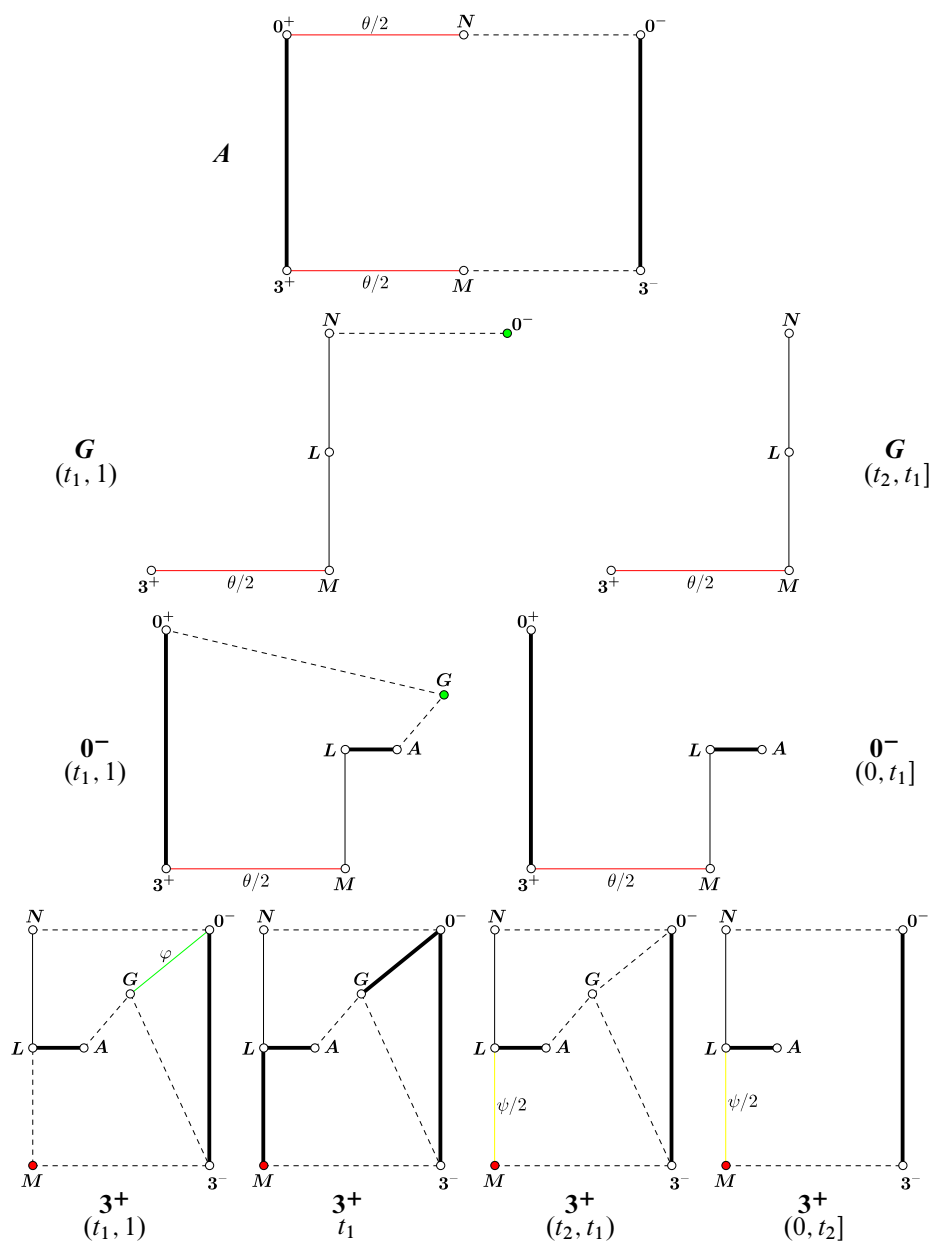
Figure 9: The generalised Coxeter diagrams of some walls of Q_t. Specifically, that of A for $t \in (0, 1)$; G for $t \in (t_1, 1)$ and $t \in (t_2, t_1]$; $\mathbf{0^-}$ for $t \in (t_1, 1)$ and $t \in (0, t_1]$; $\mathbf{3^+}$ for $t \in (t_1, 1)$, $t = t_1$, $t \in (t_2, t_1)$ and $t \in (0, t_2]$. The red and green vertices indicate the (two-dimensional) faces in Q_t with nonright dihedral angles $\frac{\theta}{2}$ and φ, coherently with Figure 7. The green, red and yellow edges indicate the edges of the wall with varying dihedral angle φ, $\frac{\theta}{2}$ and $\frac{\psi}{2}$.

with its projection $P(v)$ in the time-like hyperplane $W^\perp$, using the formula

$$P(v) = v - \frac{\langle v, W \rangle}{\langle W, W \rangle} W.$$

We then calculate the new values of α on every pair $P(v)$, $P(w)$ instead of v, w. This will determine the labels on the edges of $D_{W,t}$.

Given the abundance of right angles, in most cases α remains unaffected. More specifically:

- A is orthogonal to all the incident walls, hence $P(v) = v$ for every such wall v and all the values α remain unaffected: the diagram $D_{A,t}$ is just a subdiagram of D_t and is shown in Figure 9, first line, for all $t \in (0, 1)$.

- G is orthogonal to all the incident walls except 0^-, which is however orthogonal to all the walls incident to both G and 0^-: this implies easily that all the values $\alpha \leq 1$ remain unaffected also in this case; hence $D_{G,t}$ is just a subdiagram of D_t as in Figure 9, second line, for the times $(t_1, 1)$ and $(t_2, t_1]$, respectively.

- 0^- is orthogonal to all the incident walls except G, which is orthogonal to all the walls incident to both 0^- and G: again the values $\alpha \leq 1$ are unaffected and $D_{0^-,t}$ is a subdiagram of D_t as in Figure 9, third line, for the times $(t_1, 1)$ and $(0, t_1]$, respectively.

- 3^+ is orthogonal to all the incident walls except M, which is in turn not orthogonal to L; this is the only label that changes from Figure 7 to 9, namely that of the edge connecting M and L. We have

$$P(L) = L, \quad P(M) = M + \frac{2t^2}{t^2 + 1} 3^+$$

and we easily deduce that

$$\langle P(M), P(L) \rangle = -1, \quad \langle P(M), P(M) \rangle = 2\frac{1 - t^2}{1 + t^2}, \quad \langle P(L), P(L) \rangle = 2$$

and therefore

$$\alpha = \frac{\sqrt{1 + t^2}}{2\sqrt{1 - t^2}} = \frac{1 + t^2}{2\sqrt{1 - t^4}}.$$

In particular,

(1) when $t \in (t_1, 1)$ we have $\alpha > 1$ and the faces are ultraparallel;

(2) when $t = t_1$ we have $\alpha = 1$ and the faces are asymptotically parallel;

(3)   when $t \in (0, t_1)$ the faces meet at a dihedral angle $\frac{\psi}{2}$ that satisfies

$$\cos \frac{\psi}{2} = \frac{\sqrt{1+t^2}}{2\sqrt{1-t^2}} = \frac{1+t^2}{2\sqrt{1-t^4}}.$$

The diagram $D_{\mathbf{3^+},t}$ is shown in Figure 9, fourth line, at all times.

We note that

$$\cos \psi = 2\cos^2 \frac{\psi}{2} - 1 = \frac{1+t^2}{2(1-t^2)} - 1 = \frac{1-3t^2}{2(t^2-1)}.$$

The proof is complete. □

We can now easily draw the walls A, G, $\mathbf{0^-}$ and $\mathbf{3^+}$ of Q_t at all times.

Corollary 3.7   *The combinatorics and geometry of the polyhedra A, G, $\mathbf{0^-}$ and $\mathbf{3^+}$ of Q_t is shown in Figure 10. In particular, they all have finite volume.*

Proof   All the strata of each acute-angled polyhedron are easily deduced from its corresponding Coxeter diagram, using the algorithms described in Section 2.2, which allow one to determine first the edges and then the vertices of each polyhedron.

Recall in particular that every finite vertex arises from a triple of nodes of the Coxeter diagram of elliptic type, and every ideal vertex arises from a triple or 4–tuple of vertices of Euclidean type. The reader is invited to check that the vertices are those shown in Figure 10, and in particular the crucial fact that every edge has two vertices as its endpoints; hence, the polyhedra have all finite volume (there are no hyperideal vertices; see Theorem 2.2).

For instance, one checks that the polyhedron A contains 6 finite vertices, which correspond to an elliptic Coxeter subdiagram with tree nodes, and an ideal vertex, which corresponds to the Euclidean Coxeter subgraph with four nodes $\{\mathbf{0^-}, \mathbf{0^+}, \mathbf{3^-}, \mathbf{3^+}\}$, which represents a rectangle.

Similarly, the polyhedron G contains some finite vertices, and one ideal vertex only at the time $t = t_1$ corresponding to the subdiagram with nodes $\{\mathbf{3^+}, L, M\}$, which represents a Euclidean triangle with angles $\frac{\pi}{2}$, $\frac{\pi}{3}$ and $\frac{\theta}{2} = \frac{\pi}{6}$. When $t < t_1$ we get $\frac{\theta}{2} > \frac{\pi}{6}$ and the triple represents a finite vertex instead. The polyhedra $\mathbf{0^-}$ and $\mathbf{3^+}$ are treated similarly. □
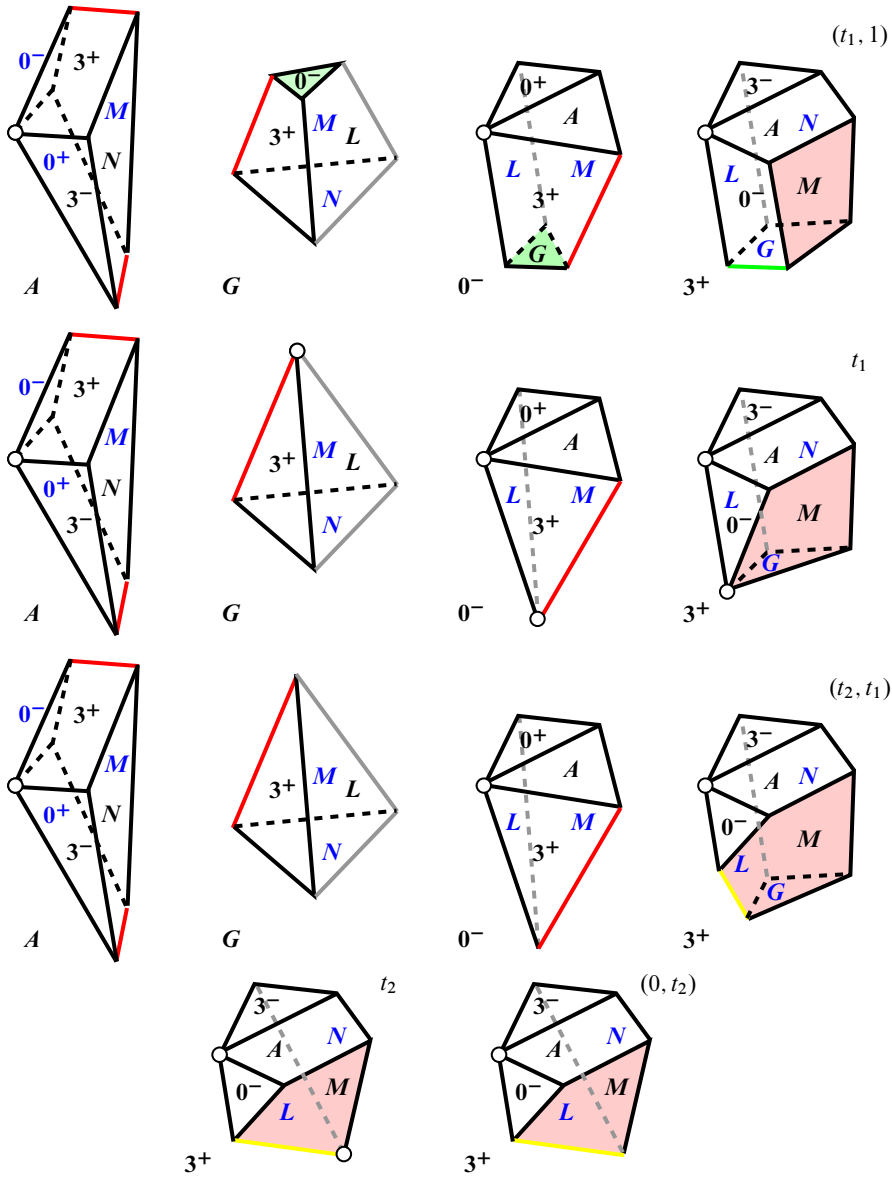
Figure 10: The walls A, G, 0^- and 3^+ of the quotient polytope Q_t at the times $(t_1, 1)$ in the first line, t_1 in the second line and (t_2, t_1) in the third line. The combinatorics of A and 0^- is constant in $(0, t_1)$, but that of 3^+ changes further at the times t_2 and $(0, t_2)$ as shown in the fourth line. Every face is labelled with the name of the adjacent wall: front faces are labelled in black and back faces in blue. On each wall, the red, green, black, grey and yellow edges have dihedral angle $\frac{\theta}{2}$, φ, $\frac{\pi}{2}$, $\frac{\pi}{3}$ and $\frac{\psi}{2}$, respectively. Similarly, on the polytope Q_t the red, green and white faces have dihedral angle $\frac{\theta}{2}$, φ and $\frac{\pi}{2}$. The ideal vertices are indicated as white dots.

Figure 10 shows both the four-dimensional dihedral angles along the faces and the three-dimensional dihedral angles of the single walls along the edges: on each wall, the red, green, black, grey and yellow edges have dihedral angle $\frac{\theta}{2}$, φ, $\frac{\pi}{2}$, $\frac{\pi}{3}$ and $\frac{\psi}{2}$, respectively. Similarly, on the polytope Q_t the red, green and white faces have dihedral angle $\frac{\theta}{2}$, φ and $\frac{\pi}{2}$. The ideal vertices are indicated as white dots.

Corollary 3.8 *The polytope Q_t has finite volume for all $t \in (0, 1]$. Its combinatorics is constant on each of the time intervals*

$$(0, t_2), \quad (t_2, t_1), \quad (t_1, 1)$$

and changes precisely at the critical times t_2, t_1 and 1.

Proof We only need to prove that Q_t has finite volume. By Theorem 2.2 it suffices to check that every edge of Q_t has two (finite or ideal) vertices as endpoints. All the edges that belong to one of the walls A, G, 0^- or 3^+ have this property, as already checked. There is yet one last edge to investigate in Figure 7, determined by the triple $\{L, M, N\}$. That edge joins the finite vertices $\{L, M, N, G\}$ and $\{L, M, N, H\}$ when $t > t_2$, and the vertices $\{L, M, N, 3^+\}$ and $\{L, M, N, 0^+\}$ when $t \le t_2$, which are ideal at $t = t_2$ and finite when $t < t_2$. □

We now finally use all the information that we gathered on the quotient polytope Q_t to analyse the original polytope P_t.

3.4 Back to the original polytope P_t

We recall that P_t has 24 walls when $t > t_2$ and 22 when $t \le t_2$, and up to the action of its symmetry group these walls reduce to four elements only,

$$\{3^+, 0^-, A, G\},$$

where G exists only for $t > t_2$. We start by showing the following.

Proposition 3.9 *For all $t \in (0, 1]$, the polytope P_t has finite volume. Moreover, its combinatorics is constant on each of the time intervals*

$$(0, t_2), \quad (t_2, t_1), \quad (t_1, 1)$$

and changes precisely at the critical times t_2, t_1 and 1. The combinatorics and geometry of the walls 3^+, 0^-, A, G is fully described in Figures 11, 12, 13 and 14.
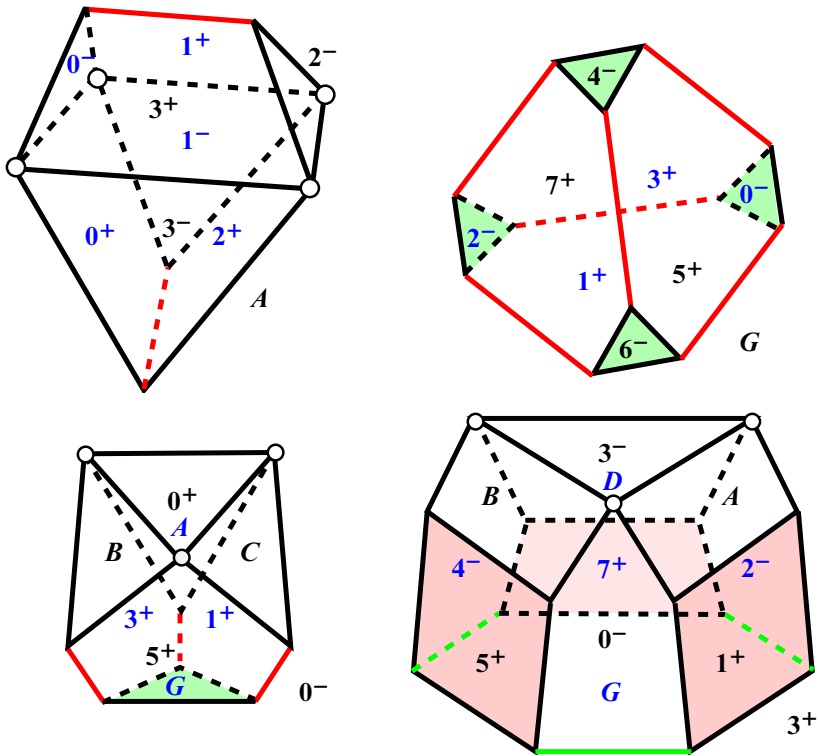
Figure 11: Combinatorial pictures of the walls A, G, 0^- and 3^+ of P_t at the times $t \in (t_1, 1)$. Every face is labelled with the name of the adjacent wall: front faces are labelled in black and back faces in blue. On each wall, the red, green and black edges have dihedral angle θ, φ and $\frac{\pi}{2}$, respectively. Similarly, on the polytope P_t the red, green and white faces have dihedral angle θ, φ and $\frac{\pi}{2}$. The ideal vertices are indicated as white dots.

Proof The walls of P_t are obtained by mirroring the corresponding walls of Q_t from Figure 10 along the faces L, M and N.   □

The figures show both the four-dimensional dihedral angles along the faces and the three-dimensional dihedral angles of the single walls along the edges. An overview of the evolving walls is shown in Figure 15.

Dihedral angles

A remarkable aspect of the deformation P_t is that most of the dihedral angles stay constantly right during the whole process. In the following proposition we write a face of P_t as a pair of intersecting walls.
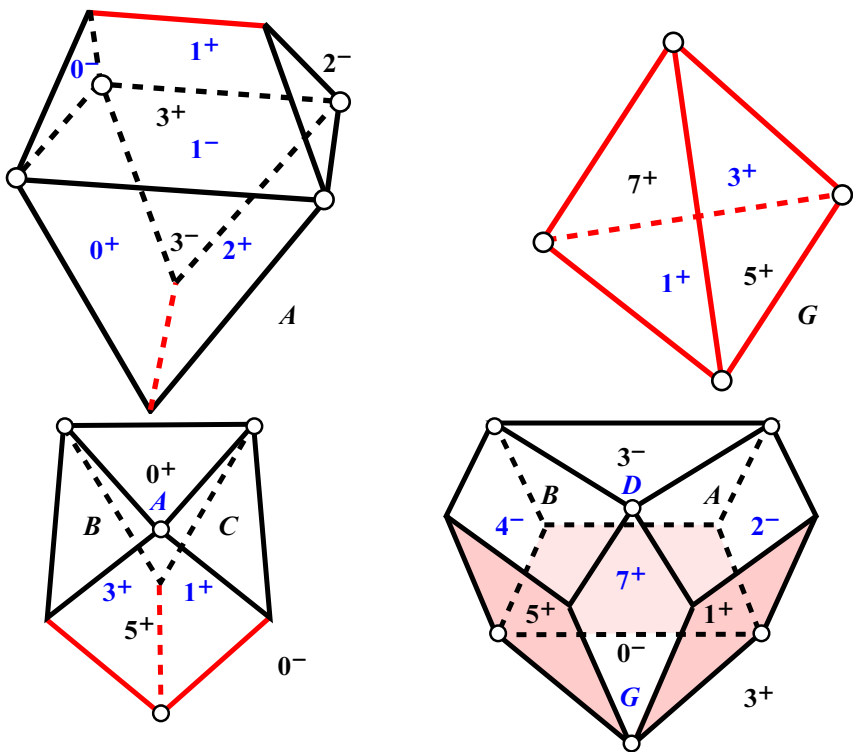
Figure 12: Combinatorial pictures of the walls A, G, 0^- and 3^+ at the critical time t_1. We use the same notations as in Figure 11. The dihedral angles are either $\frac{\pi}{3}$ (on the red faces and edges) or $\frac{\pi}{2}$ (on the rest).

Proposition 3.10 *All the faces of P_t have right dihedral angles, except:*

- *The 8 green triangles*

$$\{G, 0^-\}, \quad \{G, 2^-\}, \quad \{G, 4^-\}, \quad \{G, 6^-\},$$
$$\{H, 1^-\}, \quad \{H, 3^-\}, \quad \{H, 5^-\}, \quad \{H, 7^-\}$$

have dihedral angle φ when $t \in (t_1, 1)$.

- *The 12 red polygons*

$$\{1^+, 3^+\}, \quad \{3^+, 5^+\}, \quad \{5^+, 7^+\}, \quad \{7^+, 1^+\}, \quad \{1^+, 5^+\}, \quad \{3^+, 7^+\},$$
$$\{2^+, 0^+\}, \quad \{0^+, 4^+\}, \quad \{4^+, 6^+\}, \quad \{6^+, 2^+\}, \quad \{2^+, 4^+\}, \quad \{0^+, 6^+\}$$

have dihedral angle θ for all $t \in (0, 1)$.

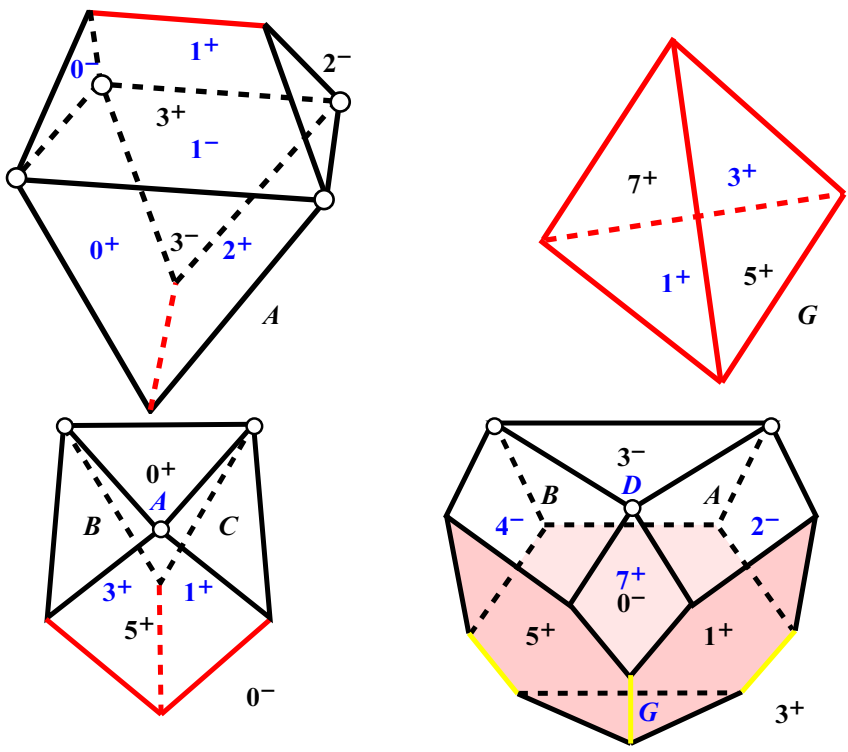*The evolution of the green and red faces is shown in Figure 16.*

Figure 13: Combinatorial pictures of the walls A, G, 0^- and 3^+ at the times $t \in (t_2, t_1)$. We use the same notations as in Figure 11. The dihedral angles are either θ (on the red faces and edges), ψ (on the yellow edges) or $\frac{\pi}{2}$ (on the rest).

It is remarkable that for all $t \in (t_1, 1)$ the non-right-angled faces intersect only in pairs at some vertices. Where this happens, the dihedral angle φ or θ of one face equals the interior angle of the other; see Figure 16.

Corollary 3.11 *The polytope P_t is acute-angled precisely when $t \geq \bar{t} = \sqrt{1/3}$.*

The polytope $P_{\bar{t}}$ is right-angled. We will soon determine the Coxeter polytopes in the family P_t.

Simple polytopes

During our analysis we have also proved the following.

Proposition 3.12 *The polytope P_t is simple for all $t \in (0, 1]$.*
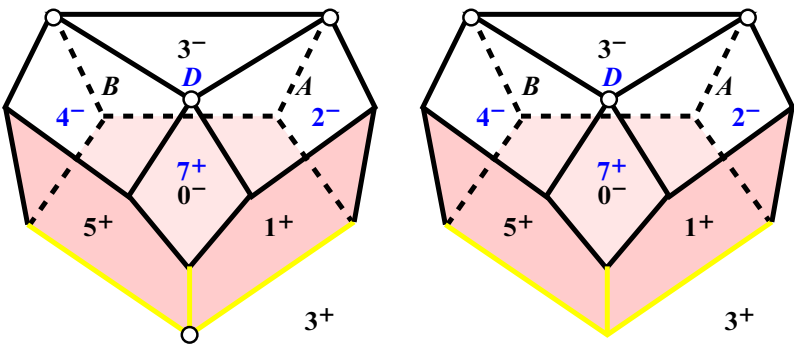
Figure 14: Combinatorial pictures of the wall 3^+ at the critical time t_2 and in the interval $t \in (0, t_2)$. We use the same notations as in Figure 11. The four-dimensional and three-dimensional dihedral angles are either θ (on the red faces), ψ (on the yellow edges) or $\frac{\pi}{2}$ (on the rest). The only nonright angle of each red pentagon is at the bottom vertex. The only difference between the two figures is the bottom vertex, which is either ideal (left) or finite (right).
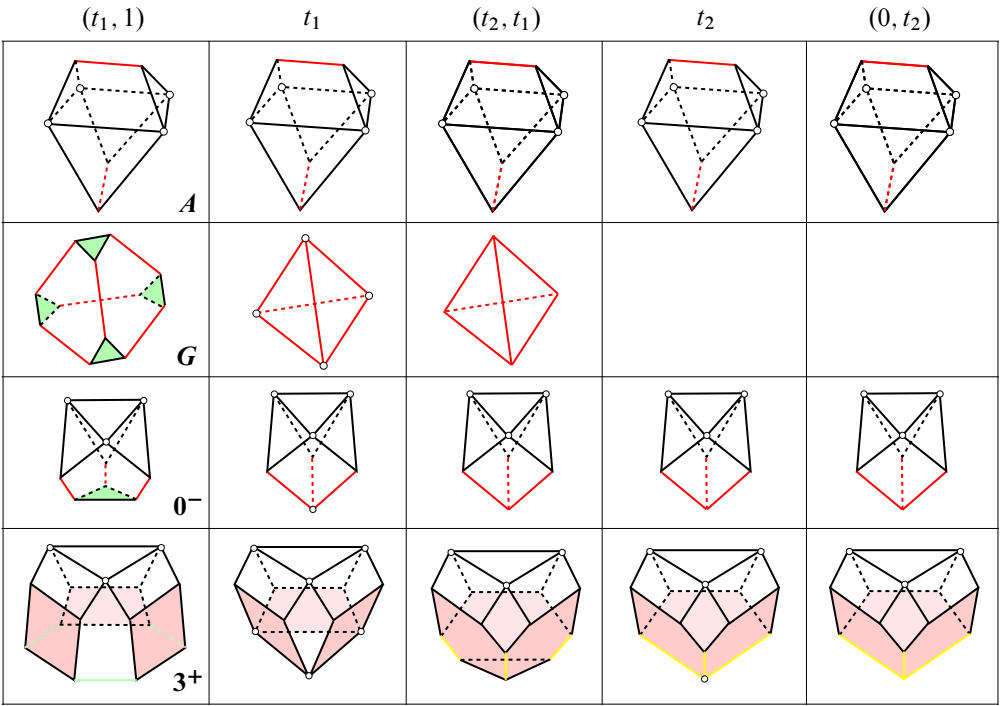

Figure 15: An overview of the combinatorics of the evolving walls. At the initial time $t = 1$ all the walls are regular ideal octahedra.

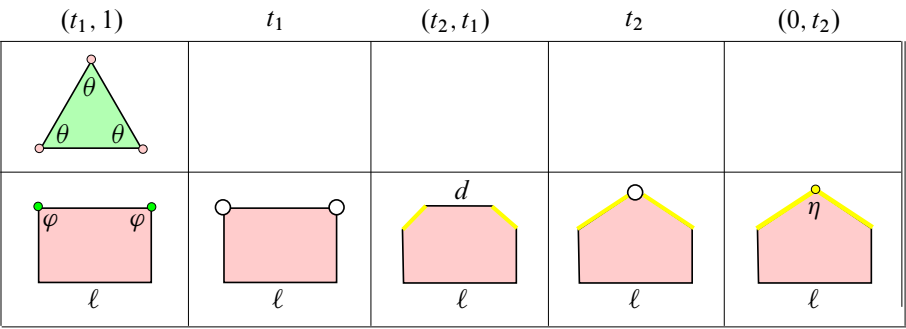| $(t_1, 1)$	t_1	(t_2, t_1)	t_2	$(0, t_2)$

Figure 16: The evolving green and red faces. The green face is an equilateral triangle and exists only for $t \in (t_1, 1)$. Vertices with big white dots are ideal. All the finite vertices are right-angled, except those labelled with some explicit angle θ, φ, or η. The angles θ, φ, η and the lengths ℓ, d depend on t. All the red faces are symmetric with respect to a vertical axis. A small green or red dot indicates the presence of an incident green or red face.

Proof The polytope P_t is acute-angled and hence [27, Section 3] simple for all $t \geq \sqrt{1/3}$. If $t < \sqrt{1/3}$, the polytope P_t has the same combinatorics of $P_{t_2 - \varepsilon}$ and is hence also simple.   □

We are now interested in the links of the vertices of the polytope P_t. The initial polytope P_1 is the ideal 24–cell: it has 24 ideal vertices, each with a Euclidean cube as a link. We now study separately the first time interval $(t_1, 1)$, the first critical time t_1, the second time interval (t_2, t_1) and the last time interval $(0, t_2]$. (The discussion for $(0, t_2]$ also includes the second critical time t_2.)

The first time interval

When $t \in (t_1, 1)$, the combinatorial change from the 24–cell P_1 consists in the substitution of 12 ideal vertices with 12 quadrilateral red faces. Each of these new 12 red faces is the intersection (with dihedral angle θ) of two positive walls that were asymptotically parallel in P_1.

Geometrically, all the other faces remain right-angled except six green triangles that were right-angled in the ideal 24–cell P_1 and have now dihedral angle φ.

Proposition 3.13 *When $t \in (t_1, 1)$, the polytope P_t has 24 walls, 108 faces, 144 edges and 60 vertices. The combinatorics can be recovered from Figure 11. In particular, the vertices are of three kinds:*
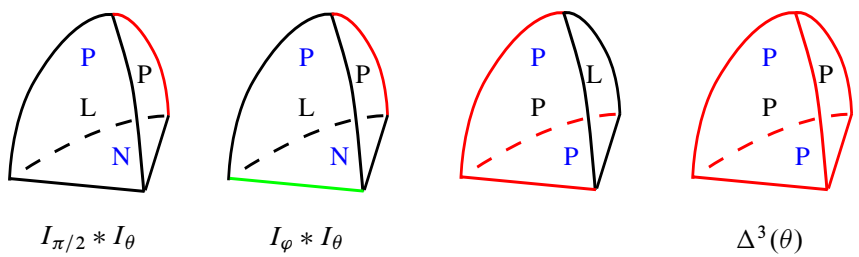
$$I_{\pi/2} * I_\theta \qquad I_\varphi * I_\theta \qquad \qquad \qquad \Delta^3(\theta)$$

Figure 17: The links of the finite vertices of the polytope P_t are spherical tetrahedra. The black, red and green edges have dihedral angle $\frac{\pi}{2}$, θ and φ, respectively. The faces of these tetrahedra are labelled (front faces in black, back faces in blue) with the type of the corresponding wall of P_t: P for positive, N for negative and L for letter. The first two tetrahedra are spherical joins of segments $I_{\pi/2} * I_\theta$ and $I_\varphi * I_\theta$, where $I_\alpha \subset S^1$ indicates a circular arc of length α. The last is the regular spherical tetrahedron $\Delta^3(\theta)$ with dihedral angles θ.

(1) 12 *ideal vertices (which actually exist for all $t \in (0, 1]$), whose link is a Euclidean rectangular parallelepiped, represented in* Figure 18, *left. For every odd $i \in \{0, \dots, 7\}$ there are three ideal vertices of type*

$$\partial_\infty i \cap \partial_\infty i^- \cap \partial_\infty j^+ \cap \partial_\infty j^- \cap \partial_\infty X \cap \partial_\infty Y$$

for some even j and some letter walls X and Y of type $A, \dots, F$.

(2) 24 *finite vertices, whose link is the spherical tetrahedron $I_{\pi/2} * I_\theta$ represented in* Figure 17. *Each of these vertices is the intersection of two positive walls, a negative wall and a letter wall of type $A, \dots, F$.*

Figure 18: The Euclidean links of the ideal vertices of the polytope P_t. The conventions as the same of Figure 17. Left: a rectangular parallelepiped, whose edge lengths vary smoothly on t. Centre: a prism with equilateral base and appears only at the time t_1, when the red edges have dihedral angle $\theta = \frac{\pi}{3}$. Right: a regular tetrahedron and it appears only at the time t_2 when the red edges have dihedral angle θ with $\cos \theta = \frac{1}{3}$.

(3) 24 *finite vertices, whose link is the spherical tetrahedron $I_\varphi * I_\theta$ represented in* Figure 17. *Each of these vertices is the intersection of two positive walls, a negative wall and a wall G or H.*

Proof The 48 finite vertices are the 4×12 vertices of the new 12 red quadrilateral faces; among these, $8 \times 3 = 24$ are also vertices of the 8 triangular green faces. Recall that the polytope P_t is simple. The links of the finite vertices are therefore tetrahedra, whose dihedral angles are all right except those corresponding to red or green faces.

The ideal vertex of the quotient polytope Q_t is (see Figure 7)

$$\partial_\infty \mathbf{3^+} \cap \partial_\infty \mathbf{3^-} \cap \partial_\infty \mathbf{0^+} \cap \partial_\infty \mathbf{0^-} \cap \partial_\infty A \cap \partial_\infty L.$$

Its link is a product of three intervals, that is, a Euclidean rectangular parallelepiped. Letting the group of symmetries K act, we get the $4 \times 3 = 12$ ideal vertices of P_t. Note that since that ideal vertex exists in Q_t for all $t \in (0, 1]$, these 12 ideal vertices of P_t exist for all $t \in (0, 1]$.   □

We note in particular that the green and red faces intersect only at the 24 finite vertices of type (3).

The first critical time

At the critical time $t = t_1$, the 8 green triangular faces collapse into 8 new ideal vertices. The only nonright dihedral angle is now $\theta = \frac{\pi}{3}$, hence P_{t_1} is a Coxeter polytope.

Proposition 3.14 *The Coxeter polytope P_{t_1} has 24 walls, 100 faces, 120 edges and 44 vertices. The combinatorics can be recovered from* Figure 12. *In particular, the vertices are of three kinds:*

(1) 12 *ideal vertices, whose link is a Euclidean rectangular parallelepiped represented in* Figure 18, *left.*

(2) 8 *ideal vertices, whose link is a Euclidean right prism over an equilateral triangle, represented in* Figure 18, *centre. Each of these vertices is the ideal vertex of a negative wall, three positive walls and a wall G or H.*

(3) 24 *finite vertices, whose link is the spherical tetrahedron $I_{\pi/2} * I_\theta$ represented in* Figure 17. *Each of these vertices is the intersection of two positive walls, a negative wall and a letter wall of type $A, \dots, F$.*
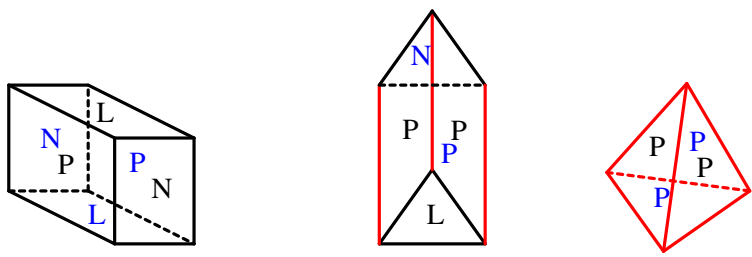
The second time interval

When $t \in (t_2, t_1)$, the combinatorial change from the Coxeter polytope P_{t_1} consists in the substitution of 8 ideal vertices with 8 new edges, drawn in yellow in Figure 13. Each yellow edge is the intersection of three positive walls, and also of three red faces. Each red face is now a right-angled hexagon.

Proposition 3.15 *When $t \in (t_2, t_1)$, the polytope P_t has 24 walls, 100 faces, 128 edges and 52 vertices. The combinatorics can be recovered from Figure 13. In particular, the vertices are of three kinds:*

(1) *12 ideal vertices, whose link is a Euclidean rectangular parallelepiped represented in Figure 18, left.*

(2) *24 finite vertices, whose link is the spherical tetrahedron $I_{\pi/2} * I_\theta$ represented in Figure 17. Each of these vertices is the intersection of two positive walls, a negative wall and a letter wall of type $\boldsymbol{A}, \ldots, \boldsymbol{F}$.*

(3) *16 finite vertices, whose link is the spherical tetrahedron represented in Figure 17, centre-right. Each of these vertices is the intersection of three positive walls and a negative wall, or three positive walls and a wall $\boldsymbol{G}$ or $\boldsymbol{H}$.*

The last time interval

When $t \in (0, t_2]$, the polytope P_t coincides with the $\mathcal{F}_t$ of [13]. At the critical time t_2, the walls $\boldsymbol{G}$ and $\boldsymbol{H}$ collapse into two new ideal vertices, which become finite as soon as $t < t_2$. Indeed, the vectors defining $\boldsymbol{G}$ and $\boldsymbol{H}$ transform from space-like to light-like and then time-like. The combinatorial change at t_2 is the inverse operation of a truncation.

The two new vertices in P_t are quadruple intersections of positive walls. Their link is a regular tetrahedron with dihedral angles θ. At $t = t_2$ the two new vertices are ideal, we have $\cos \theta = \frac{1}{3}$ and the link is a regular Euclidean tetrahedron; as soon as $t < t_2$ the angle θ increases and the link is a regular spherical tetrahedron.

Proposition 3.16 *When $t \in (0, t_2]$, the polytope P_t has 22 walls, 92 faces, 116 edges and 46 vertices. The combinatorics can be recovered from Figure 14 for positive walls and from Figure 13 for the other walls. In particular, the vertices are of four kinds:*

(1) *12 ideal vertices, whose link is a Euclidean rectangular parallelepiped represented in Figure 18, left.*

(2)　24 *finite vertices, whose link is the spherical tetrahedron* $I_{\pi/2} * I_\theta$ *represented in Figure 17. Each of these vertices is the intersection of two positive walls, a negative wall and a letter wall of type* $A, \ldots, F$.

(3)　8 *finite vertices, whose link is the spherical tetrahedron represented in Figure 17, centre-right. Each of these vertices is the intersection of three positive walls and a negative wall.*

(4)　2 *vertices, ideal for* $t = t_2$ *and finite for* $t < t_2$, *whose link is the regular tetrahedron represented in Figures 18, right, and* $17 (\Delta^3(\theta))$, *respectively. Each of these vertices is the intersection of four positive walls of the same parity.*

Note that in this time interval, the (yellow) angle

$$\psi = \arccos\left(\frac{\cos\theta}{1 - \cos\theta}\right)$$

of Lemma 3.6 equals the inner angle of a face of a regular spherical tetrahedron with dihedral angles θ. In the polytope P_t, the red faces are now pentagons with four right angles and a new angle η, that must equal the length of an edge of such a spherical tetrahedron.

Proposition 3.17 *When* $t \in (0, t_2]$, *the inner angle* η *between the two yellow edges of each red face is such that*

$$\cos\eta = \frac{\cos\theta}{1 - 2\cos\theta} = \frac{3t^2 - 1}{3 - 5t^2}.$$

First proof　Denote by P the orthogonal projection of $\mathbb{R}^{1,4}$ onto the vector subspace $W^\perp = (\mathbf{3^+})^\perp \cap (\mathbf{7^+})^\perp$, where W is generated by the vectors $\mathbf{3^+}$ and $\mathbf{7^+}$. An orthogonal basis for W is given by $\mathbf{u}_1 = \mathbf{3^+}$ and $\mathbf{u}_2 = \mathbf{7^+} + \cos\theta\, \mathbf{3^+}$. Therefore, denoting by P_i the orthogonal projection onto the subspace $\mathbb{R}\mathbf{u}_i$ for $i = 1, 2$, for every $\mathbf{v} \in \mathbb{R}^{1,4}$,

$$P(\mathbf{v}) = \mathbf{v} - P_1(\mathbf{v}) - P_2(\mathbf{v}).$$

The angle η is thus given applying (1) to the vectors

$$P(\mathbf{1^+}) = \mathbf{1^+} + \cos\psi\, \mathbf{3^+} + \cos\psi\, \mathbf{7^+}, \quad P(\mathbf{5^+}) = \mathbf{5^+} + \cos\psi\, \mathbf{3^+} + \cos\psi\, \mathbf{7^+}. \quad \square$$

Second proof　For every $n > 1$, denote by G_n the Gram matrix of a regular spherical n–simplex with dihedral angles θ, that is the $(n + 1) \times (n + 1)$ matrix with ones on

the diagonal and $-\cos\theta$ on the other entries. As we said, η is the length of an edge of a regular spherical 3–simplex with dihedral angles θ. By the sine law [6] we get

$$\frac{\sin^2\eta}{\sin^2\theta} = \frac{\det(G_3)}{\det(G_2)^2} = \frac{1 - 3\cos\theta}{(1 - 2\cos\theta)^2(1 + \cos\theta)}.$$

This easily implies the statement. □

The angle η tends to $\arccos\left(-\frac{1}{3}\right)$ as $t \to 0$.

The fixed ideal cuboctahedron

Let $\mathbb{H}^3 \subset \mathbb{H}^4$ be the hyperplane $\{x_4 = 0\}$ defined by the space-like vector $(0, 0, 0, 0, 1)$.

Lemma 3.18 *The* 12 *ideal vertices of* P_t *that exist for all* $t \in (0, 1]$ *are all in* $\partial_\infty\mathbb{H}^3$ *and do not depend on* t.

Proof Recall Section 3.2 and the quotient polytope Q_t. The fixed points of the roll symmetry R form a 2–plane contained in $\mathbb{H}^3$. The roll symmetry R fixes the ideal vertex of Q_t that exists for all t. The hyperplanes L, M and N are orthogonal to $\mathbb{H}^3$. Therefore, letting the group K act, we get that the 12 ideal vertices are contained in $\partial_\infty\mathbb{H}^3$.

Now, by solving a simple linear system in $\mathbb{R}^{1,4}$, we get

$$\mathbf{3^+}^\perp \cap \mathbf{3^-}^\perp \cap \mathbf{0^+}^\perp \cap \mathbf{0^-}^\perp \cap \mathbf{A}^\perp \cap \mathbf{B}^\perp = (\sqrt{2}, 1, 1, 0, 0)\mathbb{R},$$

showing that the ideal vertex

$$\partial_\infty\mathbf{3^+} \cap \partial_\infty\mathbf{3^-} \cap \partial_\infty\mathbf{0^+} \cap \partial_\infty\mathbf{0^-} \cap \partial_\infty\mathbf{A} \cap \partial_\infty\mathbf{B}$$

does not depend on t, nor hence the other 11 by symmetry. □

Proposition 3.19 *The intersection* $P_t \cap \mathbb{H}^3$ *does not depend on* t *and is an ideal, right-angled cuboctahedron. The quadrilateral faces are* $X \cap \mathbb{H}^3$ *for every letter wall* $X \in \{A, \ldots, F\}$, *while the triangular faces are the* 2–*faces of* P_t *given by* $i \cap i^-$ *for every* $i \in \{0, \ldots, 7\}$. *Moreover, we have* $P_t \cap \mathbb{H}^3 = P_0 = \bigcap_s P_s$.

Proof For every $t \in (0, 1]$ we have $\partial_\infty A \subset \partial_\infty\mathbb{H}^3$. Thus $A \cap \mathbb{H}^3$ must be the ideal quadrilateral containing the ideal points of A. It is easy to see that the hyperplanes containing the walls $\mathbf{0^-}$, $\mathbf{0^+}$ and $\mathbb{H}^3$ intersect in the same 2–plane. Therefore the ideal triangle $\mathbf{0^-} \cap \mathbf{0^+}$ is contained in $\mathbb{H}^3$.

By the previous lemma, such ideal polygons do not depend on t. As before, since $\mathbb{H}^3$ is orthogonal to the hyperplanes L, M and N, it suffices to let the group K act to conclude the same for the other walls.

Finally, since P_0 is the convex hull of its (ideal) vertices, that are fixed, the last statement is proved.   □

All these intersections do not depend on t. Moreover, $X \perp \mathbb{H}^3$ for all $t \in (0, 1]$ and every $X \in \{A, \dots, F\}$. What varies is the (acute) angle of intersection between $\mathbb{H}^3$ and the numbered hyperplanes:

Proposition 3.20 *The letter hyperplanes are orthogonal to the hyperplane $\mathbb{H}^3$ for all $t \in [0, 1]$. Moreover, for every $i \in \{0, \dots, 7\}$, the functions* $\mathrm{Angle}(i, \mathbb{H}^3)$ *and* $\mathrm{Angle}(i^-, \mathbb{H}^3)$ *are strictly monotone in t, they take the value $\frac{\pi}{4}$ at $t = 1$, and*

$$\lim_{t \to 0} \mathrm{Angle}(i^+, \mathbb{H}^3) = 0, \quad \lim_{t \to 0} \mathrm{Angle}(i^-, \mathbb{H}^3) = \tfrac{\pi}{2}.$$

Proof These assertions can be verified as usual by formula (1).   □

3.5 Coxeter polytopes

The dihedral angles θ and φ are strictly monotone in t. We have

$$\lim_{t \to 1} \theta(t) = 0, \quad \theta(t_1) = \tfrac{\pi}{3}, \quad \theta\big(\sqrt{1/3}\big) = \tfrac{\pi}{2},$$
$$\lim_{t \to 0} \theta(t) = \pi, \quad \varphi(1) = \tfrac{\pi}{2}, \quad \lim_{t \to t_1} \varphi(t) = 0.$$

In particular the polytope P_t is Coxeter at the times

$$1, \quad t_1 = \sqrt{3/5}, \quad \bar{t} = \sqrt{1/3}.$$

The polytope P_t is right-angled both at times $t = 1$ and $t = \bar{t}$. Note that in P_1 all vertices are ideal, while $P_{\bar{t}}$ contains both ideal and finite vertices and is quite interesting. The Coxeter polytope P_{t_1} has dihedral angles $\frac{\pi}{2}$ and $\frac{\pi}{3}$.

The orbifold Euler characteristic of these Coxeter polytopes is calculated below (for the 24–cell P_1, it is well known that $\chi(P_1) = 1$).

Proposition 3.21 *The Coxeter polytope P_{t_1} has Euler characteristic $\chi(P_{t_1}) = 1$.*

Proof The isomorphism classes of the stabilisers are obtained from the information about the dihedral angles of the faces of every dimension, that are either $\frac{\pi}{3}$, $\frac{\pi}{2}$ or 0.

Precisely, Figure 12 and Proposition 3.14 give

- 24 walls (with stabiliser $\mathbb{Z}/2\mathbb{Z}$);
- 88 faces with stabiliser $\mathbb{Z}/2\mathbb{Z} \times \mathbb{Z}/2\mathbb{Z}$;
- 12 faces with stabiliser the dihedral group D_3 (of order 6);
- 72 edges with stabiliser $\mathbb{Z}/2\mathbb{Z} \times \mathbb{Z}/2\mathbb{Z} \times \mathbb{Z}/2\mathbb{Z}$;
- 48 edges with stabiliser $D_3 \times \mathbb{Z}/2\mathbb{Z}$;
- 24 finite vertices with stabiliser $D_3 \times \mathbb{Z}/2\mathbb{Z} \times \mathbb{Z}/2\mathbb{Z}$;
- 20 ideal vertices (with infinite stabiliser).

Therefore, we get

$$\chi = 1 + 24 \cdot \left(-\tfrac{1}{2}\right) + 88 \cdot \tfrac{1}{4} + 12 \cdot \tfrac{1}{6} + 72 \cdot \left(-\tfrac{1}{8}\right) + 48 \cdot \left(-\tfrac{1}{12}\right) + 24 \cdot \tfrac{1}{24}$$
$$= 1 - 12 + 22 + 2 - 9 - 4 + 1 = 1.$$

The proof is complete. $\qquad\square$

We will reprove that $\chi(P_{t_1}) = \chi(P_1) = 1$ later on using two more different arguments.

Proposition 3.22 *The Coxeter polytope $P_{\bar{t}}$ has Euler characteristic $\chi(P_{\bar{t}}) = \tfrac{5}{8}$.*

Proof This is easier than above: since the polytope is right-angled, the stabiliser of a k–dimensional face is isomorphic to $(\mathbb{Z}/2\mathbb{Z})^{4-k}$. Therefore Proposition 3.16 gives

$$\chi = 1 + 22 \cdot \left(-\tfrac{1}{2}\right) + 92 \cdot \tfrac{1}{4} + 116 \cdot \left(-\tfrac{1}{8}\right) + 34 \cdot \tfrac{1}{16} = \tfrac{1}{8}(8 - 88 + 184 - 116 + 17) = \tfrac{5}{8},$$

and the proof is complete. $\qquad\square$

There are also two more interesting times t when θ equals $\tfrac{2\pi}{5}$ and $\tfrac{2\pi}{3}$. In both cases the resulting P_t is however not a Coxeter polytope, because the angles do not divide π.

3.6 Volume

We now study the volume $\mathrm{Vol}(P_t)$ of the polytope P_t. Instead of a long computation using the Poincaré formula, we just exhibit the value of the volume and verify it by the Schläfli formula. Recall that the Schläfli formula can be applied only while the combinatorics stays constant, therefore we need to consider three cases separately,

for the first, second and last time interval. We know the initial data of these three differential equations, because the Gauss–Bonnet formula for 4–orbifolds

$$\mathrm{Vol}(O) = \frac{4\pi^2}{3}\chi(O)$$

furnishes the volume of the Coxeter polytopes P_1 and of P_{t_1}.

Instead of using t as a parameter, it is much more convenient to write $\mathrm{Vol}(P_t)$ in function of the angles θ and φ.

Proposition 3.23 *When $t \in [t_1, 1]$, the volume of P_t depends on the dihedral angles θ and φ as follows:*

$$\mathrm{Vol}(P_t) = \frac{4\pi^2}{3}\left(2 - \frac{3}{\pi}\theta - \frac{2}{\pi}\varphi + \frac{6}{\pi^2}\theta\varphi\right).$$

Proof By Proposition 3.10 the only nonconstant dihedral angles are

- θ at 12 red quadrilateral faces with angles $\frac{\pi}{2}, \frac{\pi}{2}, \varphi, \varphi$;
- φ at 8 green triangular faces with angles θ, θ, θ.

Therefore, the Schläfli formula gives

$$\frac{1}{8}d\mathrm{Vol} = \left(\varphi - \frac{\pi}{2}\right)d\theta + \left(\theta - \frac{\pi}{3}\right)d\varphi.$$

The orbifold Euler characteristic of the extremes is $\chi(P_1) = 1 = \chi(P_{t_1})$. The first equality is well-known, the second is proved in Proposition 3.21. (Actually, we only need the first, and we reobtain the second now, providing a new proof of Proposition 3.21.) Hence, by Gauss–Bonnet, the initial and final value of the volume is $\frac{4}{3}\pi^2$.

It is easy to check that the formula in the statement of the proposition satisfies this Cauchy problem (recall that at the extremes the values of the angles are $\theta = 0$, $\varphi = \frac{\pi}{2}$ and $\theta = \frac{\pi}{3}$, $\varphi = 0$, respectively). By uniqueness of the solution, the statement is proved. □

In the second and last time intervals, the only nonconstant dihedral angle is θ, therefore the volume decreases with θ by the Schläfli formula. In the second time interval, the formula for the volume simplifies and becomes linear in θ.

Proposition 3.24 *When $t \in [t_2, t_1]$, the volume of P_t depends on the dihedral angle θ as follows:*

$$\mathrm{Vol}(P_t) = \frac{4\pi^2}{3}\left(2 - \frac{3}{\pi}\theta\right).$$

Proof The nonconstant dihedral angle is θ at 12 right-angled red hexagons. Therefore, the Schläfli formula gives

$$d\,\mathrm{Vol} = -4\pi\,d\theta.$$

Moreover, we know that $\mathrm{Vol}(P_{t_1}) = \frac{4}{3}\pi^2$ and $\theta(t_1) = \frac{\pi}{3}$. □

We now analyse the last time interval. Recall the final collapse as $t \to 0$.

Proposition 3.25 *When $t \in [0, t_2]$, the volume of P_t depends on the dihedral angle θ, as follows:*

$$\mathrm{Vol}(P_t) = \frac{4\pi^2}{3}\left(2 - \frac{3}{\pi}\theta + \frac{3}{\pi^2}\int_a^\theta \eta(\tilde{\theta})\,d\tilde{\theta}\right),$$

where $a = \arccos\frac{1}{3}$ and η depends on θ as prescribed by Proposition 3.17*. Moreover, the volume tends to zero as $t \to 0$.*

Proof Looking at Figure 14, the nonconstant dihedral angle is θ at the 12 red pentagons of Proposition 3.17. Therefore, the Schläfli formula gives

$$d\,\mathrm{Vol} = -4(\pi - \eta)\,d\theta.$$

We know the initial datum at $t = t_2$ from Proposition 3.24. The Schläfli formula is satisfied and the first statement is proved.

The last statement may be proved geometrically by showing that P_t collapses onto the three-dimensional P_0, with its ideal vertices staying fixed and the finite ones converging to $\mathbb{H}^3$. Alternatively, we can show that the value of the following *Coxeter integral* is

$$\int_a^\pi \arccos\left(\frac{\cos\theta}{1 - 2\cos\theta}\right)d\theta = \frac{\pi^2}{3}.$$

This integral is not easy to compute directly; we instead give a geometric argument. The Schläfli formula for a spherical polyhedron P is

$$d\,\mathrm{Vol}(P) = \frac{1}{2}\sum_i l_i\,d\alpha_i.$$

We apply that formula to the regular spherical tetrahedron T with dihedral angles θ. Recall that η is the length of an edge of T. Therefore, denoting by $V(\theta)$ the volume of T, the formula becomes
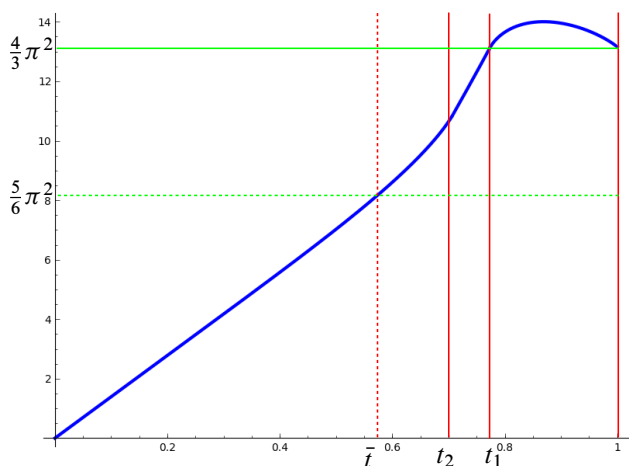
$$dV(\theta) = 3\eta\,d\theta.$$

Figure 19: The function $\mathrm{Vol}(P_t)$. The polytope P_t changes its combinatorics at the times t_2, t_1, 1 and is Coxeter at the times $\bar{t}$, t_1, 1.

Now, to get the initial and final data of the last differential equation, we analyse the limit cases where $\theta = a = \arccos \frac{1}{3}$ and $\theta = \pi$. In the first case, the tetrahedron is a point, thus

$$V(\theta) = 3 \int_a^\theta \eta(\tilde{\theta}) \, d\tilde{\theta}$$

(this is not so surprising: compare with the Poincaré formula in Section 2.1). When $\theta = \pi$, instead, the tetrahedron becomes a halfspace of S^3 (the surface of the tetrahedron becomes S^2 tessellated by four regular spherical triangles with inner angles $\psi = \frac{2\pi}{3}$), therefore

$$V(\pi) = \tfrac{1}{2}\mathrm{Vol}(S^3) = \pi^2,$$

which gives the desired value for the Coxeter integral. $\qquad\square$

Corollary 3.26 *The function $t \mapsto \mathrm{Vol}(P_t)$ is of class C^1 and shown in Figure 19.*

4 The manifolds

We now use the deforming polytopes P_t to construct some deforming hyperbolic cone four-manifolds W_t, N_t and M_t, each tessellated into a fixed number of copies of P_t. The manifolds W_t and M_t are those needed for Theorems 1.2 and 1.1.

Overview

We first construct a hyperbolic cone manifold W_t tessellated into eight copies of P_t. The manifold W_t is constructed by mirroring P_t three times, one for each wall octet; this is a particularly simple application of a colouring technique that we introduce in Section 4.1. In fact W_t is the simplest interesting cone manifold that we can construct from P_t.

The deforming cone manifold W_t has many symmetries and is relatively easy to analyse, so we do this in some detail. As usual, we think of t moving backwards from the initial time 1 in the interval $(0, 1]$. Along the path in $(0, 1]$ we discover various types of hyperbolic Dehn surgeries, and a final degeneration at $t \to 0$ similar to the one described by Thurston in his notes [25]. This proves Theorem 1.2.

When t varies in the interval $[t_1, 1]$, the manifold W_t is quite like the one needed for Theorem 1.1, except that it interpolates between a manifold and an *orbifold*. To promote the orbifold to a manifold, we need to modify the construction: we build a new cone manifold deformation N_t via a more complicated pattern, and then further quotient it to get the M_t of Theorem 1.1.

The cone manifolds W_t, M_t and N_t that we construct here are not special in any sense: there are many ways one can modify their construction to produce different deforming cone manifolds from P_t with different types of behaviour. By taking finite covers, one can also get infinitely many examples of various kinds. The only difficulty in the overall process is, of course, that we are working in dimension four and hence the combinatorial patterns are more complicated than in dimension three.

4.1 The colouring technique

How can we construct a hyperbolic cone manifold from a single polytope P? A simple method consists of colouring its walls and then mirroring P iteratively along them.

That is, we take a palette $\{c_1, \ldots, c_k\}$ of colours and assign arbitrarily a colour to every wall of P (we suppose that each colour c_i is assigned to P at least once); then we mirror P iteratively k times along its walls, one colour at a time.

More specifically, for every $I = (i_1, \ldots, i_k) \in \{0, 1\}^k$ we fix a copy P^I of P, and we identify every point in a wall of P^I coloured with c_i with the corresponding point in $P^{I'}$, where I' differs from I only in its ith coordinate.

The resulting space is a hyperbolic cone manifold M tessellated into 2^k copies of P. If P is right-angled and all pairs of adjacent walls have different colours, then M is a hyperbolic manifold (with no singularities).
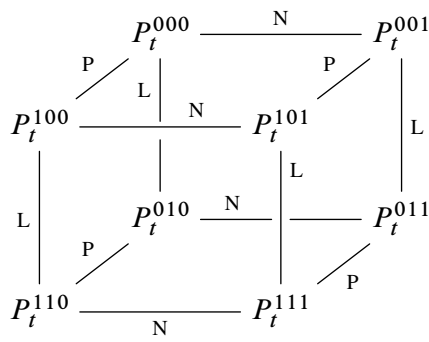
This construction works in all dimensions and was used for instance in [15] with the standard three-colouring of the ideal 24–cell P_1. It is now natural to extend it to P_t for all $t \in (0, 1]$.

4.2 A family W_t of hyperbolic cone four-manifolds

We now apply the colouring technique to our family P_t of deforming polytopes for all $t \in (0, 1]$.

Each polytope P_t in the family has either 24 or 22 walls, partitioned into *letter*, *negative* and *positive* walls. We interpret this as a colouring of the walls of P_t with three colours {L, N, P}, and we define W_t to be the space obtained from P_t by mirroring it as prescribed by this colouring, as explained above.

The space W_t is a hyperbolic cone manifold for all $t \in (0, 1]$. It is tessellated into $2^3 = 8$ copies P_t^{ijk} of P_t, whose walls are identified according to the following cubic scheme:

When $t = 1$, the polytope P_1 is the right-angled ideal 24–cell and W_1 is a nice and very symmetric hyperbolic four-manifold with 24 cusps, each cusp having a cubic 3–torus section; this hyperbolic four-manifold was first described in [15, Example 2.9]. We now study W_t when $t < 1$.

The singular set Σ

When $t < 1$, the polytope P_t is not right-angled anymore, hence some singularities appear in W_t. Luckily, only few faces in P_t are not right-angled, so the singularities are easily detected.

Proposition 4.1 *The singular set Σ of W_t is the union of the green and red faces of the eight copies of P_t.*

Proof At every point $x \in \partial P$ that does not lie in a green or red face, the polytope is locally right-angled and the adjacent walls have distinct colours. Therefore x becomes a smooth point in W_t. □

In particular, Σ is the closure of its 2–strata and we can describe it quite easily. Recall from Figure 5 the names of some elliptic cone three-manifolds. We will also use the following terminology.

Definition 4.2 We denote by $S^n(\alpha)$ the (hyperbolic, Euclidean or spherical) cone n–manifold obtained by doubling the regular (hyperbolic, Euclidean or spherical) n–simplex with dihedral angle $\frac{\alpha}{2}$ (when it exists). All the $(n-2)$–dimensional strata in $S^n(\alpha)$ have cone angle α. In the Euclidean case we have $\cos\frac{\alpha}{2} = \frac{1}{n}$ and $S^n(\alpha)$ is defined only up to rescaling.

By a *closed k–stratum* we mean the closure of a k–stratum.

Proposition 4.3 *Each closed 2–stratum of $\Sigma \subset W_t$ is either a green or red hyperbolic surface as shown in Figure 20. Its cone angle is 4φ and 2θ, respectively.*

There are 1–strata only when $t \in (0, t_1)$. The unit tangent space at a point in a 1–stratum is $S^0 * S^2(2\theta)$.

There are 0–strata only in two disjoint time intervals, and these are the following:

- *When $t \in (t_1, 1)$, there are 24 points with unit tangent space $C_{2\theta} * C_{4\varphi}$.*
- *When $t \in (0, t_2)$, there are 8 points with unit tangent space $S^3(2\theta)$.*

Proof To understand Σ, we analyse all the vertices v of P_t and determine the unit tangent space of their images in W_t. The vertices of P_t are fully described in Propositions 3.13, 3.14, 3.15 and 3.16, and we refer to them.

We analyse the finite vertices v of P_t case by case. The link of v in P_t is always some spherical tetrahedron Δ whose four faces are naturally coloured like the walls they are contained in. We refer to Figure 17.

The unit tangent space of v in M_t is obtained by mirroring Δ along its faces according to the colours.

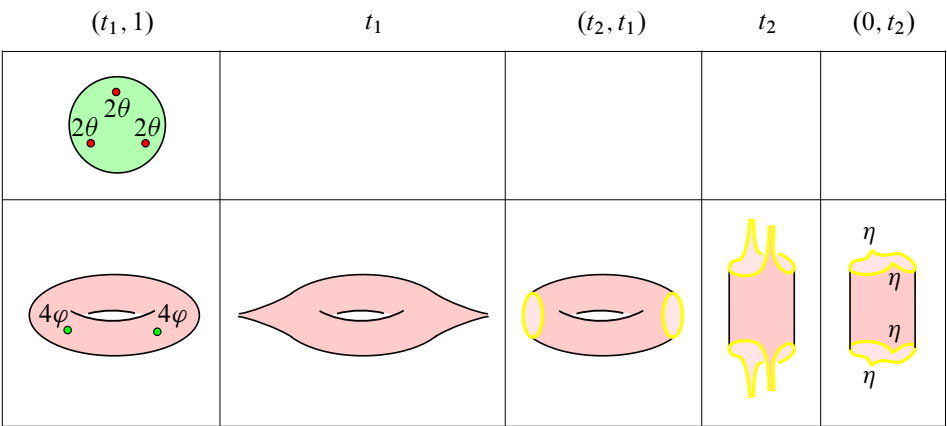| $(t_1, 1)$	t_1	(t_2, t_1)	t_2	$(0, t_2)$

Figure 20: Each closed 2–stratum of the singular set Σ of W_t is either green or red and its topology is shown here, depending on $t \in (0, 1)$. The green closed stratum is a sphere with three cone points of angle 2θ (the cone points are 0–strata) and arises only when $t > t_1$. The red closed stratum is a cone torus for $t > t_1$, a twice-punctured torus for $t = t_1$ and a compact twice-holed torus with geodesic boundary for $t \in (t_2, t_1)$; the topology of the red closed stratum changes at $t = t_2$ into an annulus: the geodesic boundary is noncompact at $t = t_2$, and two boundary cone points arise when $t \in (0, t_2)$ with some angle η.

We note that a spherical tetrahedron with 4 right dihedral angles $\frac{\pi}{2}$ and two opposite edges with dihedral angles α and β is a spherical join $I_\alpha * I_\beta$ of two circle arcs of length α and β.

(1) For every $t \in (0, 1)$ the polytope P_t has 24 finite vertices v with link the spherical join $\Delta = I_\theta * I_{\pi/2}$. The four faces of Δ are coloured as P, P, N, L, with

   • the edge $I_{\pi/2}$ lying between the two faces coloured by P, that form a dihedral angle θ, and

   • the edge I_θ lying between N and L, that form a dihedral angle $\frac{\pi}{2}$.

   By mirroring Δ along L we get $I_\theta * I_\pi$ and by then mirroring along N we get $I_\theta * S^1$. Finally, by mirroring the result along P we get $C_{2\theta} * S^1$. Therefore the vertex v in W_t is an interior point of some 2–stratum of Σ.

(2) When $t \in (t_1, 1)$ the polytope P_t has 24 vertices v with link $I_\theta * I_\varphi$. Similarly as before, the resulting unit tangent space in W_t is $C_{2\theta} * C_{4\varphi}$.

(3) When $t \in (0, t_1)$, the polytope P_t contains some (either 16 or 8) vertices v with link a spherical tetrahedron with three edges sharing a vertex having dihedral

angle θ, while the other three have dihedral angle $\frac{\pi}{2}$. Three faces are coloured with P and one with either N or L. By mirroring along N or L we get $S^0 * T$, where T is the equilateral spherical triangle with inner angles θ. By mirroring the result along P we get $S^0 * S^2(2\theta)$. Therefore v in W_t belongs to the 1–stratum of Σ.

(4) When $t \in (0, t_2]$, the polytope P_t contains 2 vertices v with link a spherical regular tetrahedron with all dihedral angles θ and all faces coloured by P. By mirroring it we get $S^3(2\theta)$.

This discussion determines the possible unit tangent spaces at every point of W_t for all times $t \in (0, 1)$, since the vertices contain all the relevant information.

The 2–strata in Figure 20 are obtained by analysing the effect of the mirroring to the green and red polygons of Figure 16. Each side e of every green or red polygon f is naturally coloured by the colour of the unique wall that is incident to e but does not contain f (every edge in a simple polytope is incident to three walls). By applying the mirroring technique we get the 2–stratum. Here are the details:

• The three sides of the green triangles are coloured with P, the triangle is mirrored and gives a green sphere $S^2(2\theta)$ with three cone points of angle 2θ, and this is a closed 2–stratum.

• The horizontal and vertical sides of the red polygon in Figure 16 are coloured by L and N, so at $t > t_1$ the polygon is a quadrilateral and is mirrored twice to give a torus with two cone points of angle 4φ, and each torus is tessellated by four rectangles and forms a closed stratum; when $t < t_1$, the diagonal sides are coloured with P and are not mirrored: they form the (yellow) boundary of the 2–stratum (which consists of closed 1–strata).

The proof is complete. □

Corollary 4.4 *When $t \in (t_1, 1)$, the singular set Σ is an immersed geodesic surface made of 12 cone tori and 8 cone spheres, intersecting in 24 points.*

The intersection pattern of the red cone tori and green cone spheres is shown in Figure 21, left. The figure then shows the evolution of Σ when $t > t_2$.

Note that for all $t \in (0, 1]$ the unit tangent spaces are cone manifolds always supported on the sphere S^3. Therefore the cone manifold W_t is always supported on a four-manifold.

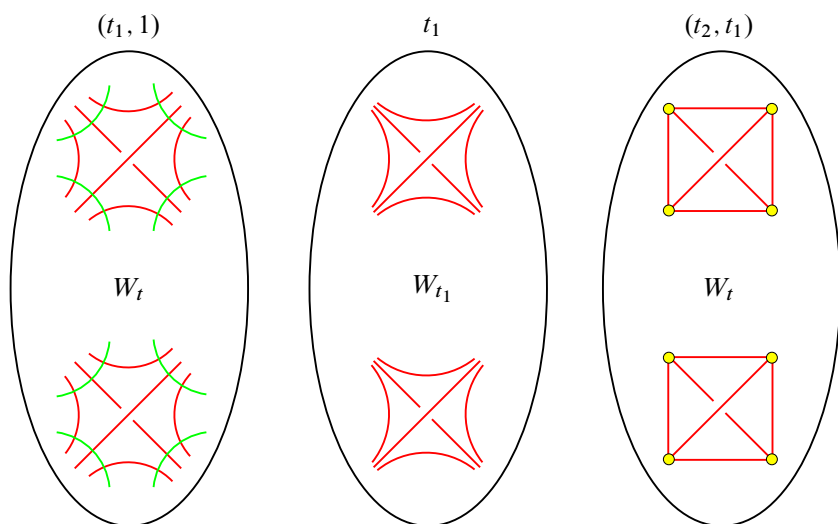Here is another important consequence of Proposition 4.3.

Figure 21: The evolution of the singular locus Σ of W_t. Left: when $t \in (t_1, 1)$, the singular locus Σ consists of 12 red cone tori (with two singular points) and 8 green cone spheres (with three singular points) that intersect transversely precisely in their 24 singular points. Centre: when $t = t_1$, the cone spheres disappear to infinity and the 12 cone tori transform into punctured tori: triples of punctures of distinct tori go to the same cusp in W_{t_1}. Right: when $t \in (t_2, t_1)$, the cusps in W_{t_1} are filled with small simple closed geodesics and each twice-punctured torus transforms into a twice-holed compact torus with geodesic boundary consisting of two of these small geodesics; twice-holed tori and closed geodesics are represented as red edges and yellow vertices, respectively. The evolution continues with the interval $(0, t_2]$, but we do not draw it here.

Corollary 4.5 When $t = t_1$, the hyperbolic cone manifold W_{t_1} is an orbifold. Its singular set Σ consists of 12 red twice-punctured tori with cone angle $\frac{2\pi}{3}$.

Proof At $t = t_1$, we have $2\theta = \frac{2\pi}{3}$.   □

We have shown that the family W_t with $t \in [t_1, 1]$ interpolates between a manifold for $t = 1$ and an orbifold for $t = t_1$. We now analyse the cusps of the whole family.

The cusps

Recall the notation introduced in [Definition 4.2](#). The *type* of a cusp is the homeomorphism type of a Euclidean cone 3–manifold section (we only determine the homeomorphism type, not the isometry type.)

Proposition 4.6 *For every $t \in (0, 1]$ the hyperbolic cone four-manifold W_t has 12 cusps of three-torus type, plus some additional cusps only at the critical times:*

- *When $t = 1$, there are 12 additional cusps of three-torus type.*
- *When $t = t_1$, there are 8 additional cusps of type $S^2\left(\frac{2\pi}{3}\right) \times S^1$.*
- *When $t = t_2$, there are 8 additional cusps of type $S^3\left(2 \arccos \frac{1}{3}\right)$.*

Proof Every ideal vertex v of P_t has a Euclidean link Δ, a Euclidean polyhedron whose faces are coloured by the walls in P_t they are contained in. Each ideal vertex of P_t gives rise to some cusps in W_t whose Euclidean sections are obtained by mirroring Δ according to the colours. We refer to Figure 18. Here are the details:

- For every $t \in (0, 1)$ the polytope P_t has 12 ideal vertices v whose link is a parallelepiped, with opposite faces coloured with P, N and L. Each parallelepiped gives rise to a cusp of three-torus type.

- When $t = 1$, the 24–cell P_1 has 12 more ideal vertices, identical to the 12 analysed above.

- When $t = t_1$, the polytope P_t has 8 additional ideal vertices, whose link is a right prism with triangular base. The two base triangles are coloured in N and L, while the lateral faces have P. By mirroring we get the 8 additional cusps of type $S^2\left(\frac{2\pi}{3}\right) \times S^1$.

- When $t = t_2$, the polytope P_t has 2 additional ideal vertices, whose link is a regular tetrahedron Δ, with all faces coloured with P. By mirroring we get 8 cusps of type $S^3\left(2 \arccos \frac{1}{3}\right)$. (If we mirror along a colour that is not there, we just take two disjoint copies of the object, and this applies here twice to the missing colours L and N.)

The proof is complete. □

The surgeries

At the critical times 1, t_1 and t_2, the cone manifold W_t changes by some surgeries that we now analyse. Recall that W_1 is a cusped hyperbolic four-manifold with 24 cusps and no singularities. As usual, we start with W_1 and we run t backwards.

Proposition 4.7 *As soon as $t < 1$, the cone manifold W_t modifies from W_1 by Dehn filling twelve cusps with twelve red cone tori.*

Topologically, each of these 12 cusps is diffeomorphic to $S^1 \times S^1 \times S^1 \times [0, +\infty)$ and is replaced by a "solid torus" $S^1 \times S^1 \times D^2$. Each new red cone torus is a core

$S^1 \times S^1 \times \{0\}$ of one such solid torus: its area, $4\pi - 8\varphi$, and its cone angle, 2θ, are both arbitrarily small when t is close to 1, and they increase as t tends to t_1, like in the familiar three-dimensional hyperbolic Dehn filling picture. When $t \to t_1$, the cone angle 2θ tends to $\frac{2\pi}{3}$.

Recall that the singular set Σ contains also 8 green cone spheres whose cone angles vary from 2π to 0 as t goes from 1 to t_1.

Proposition 4.8 *At the critical time t_1 the 8 green cone spheres are drilled and create 8 new cusps. As soon as $t < t_1$, the 8 cusps are filled with 8 yellow small closed geodesics.*

Every green cone sphere has a tubular neighbourhood homeomorphic to $S^2 \times D^2$, and the drilling substitutes it with a cusp homeomorphic to $S^2 \times S^1 \times [0, +\infty)$. Recall that we are in a cone manifold (or orbifold) context: the S^2 factor is the *flat* cone sphere $S^2\left(\frac{2\pi}{3}\right)$, hence $S^2 \times S^1$ is a flat cone three-manifold.

As soon as $t < t_1$, each such cusp is substituted with a $D^3 \times S^1$. The new core closed curve $\{0\} \times S^1$ is a small closed geodesic.

Remark 4.9 The substitution of an S^2 (with trivial normal bundle) with an S^1 is a common topological surgery in dimension four: it consists in replacing an embedded $S^2 \times D^2$ with $D^3 \times S^1$, glued along the same boundary $S^2 \times S^1$. We have just discovered an example where the surgery may be realised as a smooth path of hyperbolic cone four-manifolds. Both the cores S^2 and S^1 are geodesic all along the path. We call this path a *hyperbolic Dehn surgery* in Theorem 1.2.

A similar, but different, kind of hyperbolic surgery arises at the next critical time. We start by noticing the following:

Proposition 4.10 *When $t \in (t_2, t_1)$, the manifold W_t contains four geodesic copies of the hyperbolic cone three-manifold $S^3(2\theta)$, which collapse when $t \to t_2$. At the critical time t_2, these are drilled and create 8 new cusps. As soon as $t < t_2$, the 8 cusps are filled with 8 four-balls.*

Proof When $t \in (t_2, t_1)$, each letter wall G and H is a hyperbolic regular tetrahedron with dihedral angle θ; when mirrored in W_t, these walls form four geodesic copies of $S^3(2\theta)$. When $t \to t_2$, these walls collapse to ideal vertices, which become finite as soon as $t < t_2$.   □

Each geodesic $S^3(2\theta)$ has a tubular neighbourhood homeomorphic to $S^3 \times [-1, 1]$, and the drilling substitutes it with two cusps, each homeomorphic to $S^3 \times [0, +\infty)$. Here S^3 is the flat $S^3(2\theta)$, since $\cos(\theta) = \frac{1}{3}$ at the critical time t_2.

As soon as $t < t_2$, each cusp is filled with a D^4. We will determine the topology of W_t when $t < t_2$ in the next section.

Remark 4.11 The substitution of an S^3 (with trivial normal bundle) with an S^0 is another common topological surgery in dimension four: we substitute $S^3 \times D^1$ with $D^4 \times S^0$, glued along the same boundary $S^3 \times S^0$, and we have just discovered that it can also be realised as a smooth path of hyperbolic cone manifolds. It is also called a hyperbolic Dehn surgery in Theorem 1.2.

Remark 4.12 The topology of W_t in the last interval $(0, t_2)$ is surprisingly simple: we will show in Proposition 4.13 below that W_t is diffeomorphic to a product $C \times S^1$, where C is some cusped hyperbolic 3–manifold when $t \in (0, t_2)$.

Therefore the manifold W_t for $t \in (t_2, t_1)$ is obtained from $C \times S^1$ by a simple surgery, the replacement of four copies of S^0 with four S^3, and hence W_t is diffeomorphic to $(C \times S^1) \#_4 (S^1 \times S^3)$ when $t \in (t_2, t_1)$.

Finally, the manifold W_t for $t \in (t_1, 1)$ is obtained from the latter by one more surgery, which replaces eight copies of S^1 with eight S^2. We can build a five-dimensional film interpretation of this topological process: start with $C \times D^2$, then add four 1–handles, and eight 2–handles.

Orbifolds

We have already noted that W_t is an orbifold at $t = t_1$, whose singular locus is a surface with cone angle $\frac{2\pi}{3}$. There is also one more orbifold in the family W_t, of a quite different nature: at the time $t = \bar{t}$ the singular set Σ is a *foam* (a two-dimensional complex with generic singularities) with all cone angles π; the singularities are locally like those of the double of a right-angled polytope.

Summing up, the cone manifold W_t is an orbifold at the times

$$1, \quad t_1 = \sqrt{3/5}, \quad \bar{t} = \sqrt{1/3}.$$

These correspond to the times when P_t is a Coxeter polytope. In fact the colouring technique furnishes regular orbifold coverings such that

$$P_1 = W_1/(\mathbb{Z}/2\mathbb{Z})^3, \quad P_{t_1} = W_{t_1}/(\mathbb{Z}/2\mathbb{Z})^3, \quad P_{\bar{t}} = W_{\bar{t}}/(\mathbb{Z}/2\mathbb{Z})^3.$$
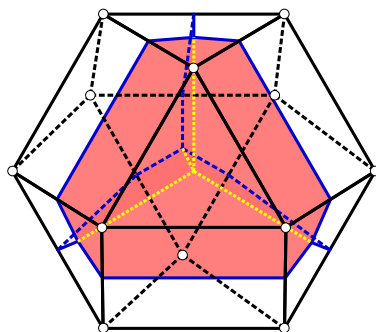
Figure 22: In the last time interval $(0, t_2)$, the four odd (or even) positive walls of the polytope P_t form an ideal right-angled cuboctahedron Q with centre v, pleated along six red pentagons. In the picture, the edges of Q are black. The faces of Q are divided as follows: (i) four ideal triangles, each a common face of an odd wall i^+ with its negative counterpart i^-; (ii) four ideal triangles, each subdivided by the red pleats into three quadrilaterals, all faces of *the same* even negative wall; (iii) six ideal quadrilaterals, each subdivided by a red pleat into two quadrilaterals, both faces of *the same* letter wall. The edges of each positive wall are coloured as follows: the black edges are contained in edges of Q, the blue edges are contained in faces of Q (they are the red edges of the even negative and letter walls in Figure 13), the yellow edges are contained in the interior of Q and intersect in the centre v of Q. Each pleating pentagon is a red face of an odd positive wall and in the picture has three blue edges and two yellow edges.

The three orbifolds W_t are arithmetic, since P_t is (see Section 3.3). Moreover,

$$\chi(W_1) = 8, \quad \chi(W_{t_1}) = 8, \quad \chi(W_{\bar{t}}) = 5$$

as a consequence of Propositions 3.21 and 3.22. We will prove in Proposition 4.13 that the underlying space of $W_{\bar{t}}$ is topologically a product $C \times S^1$.

The final degeneration

We now study W_t as $t \to 0$ and show that W_t degenerates to a hyperbolic three-manifold.

We already know that the polytope P_t tends to the three-dimensional ideal right-angled cuboctahedron P_0 shown in Figure 22. The cuboctahedron P_0 can be naturally coloured with two colours, one assigned to the triangles and the other to the quadrilaterals. Let C

be the hyperbolic three-manifold constructed from P_0 by mirroring it according to this colouring: the three-manifold C is tessellated into four copies of P_0 and we call it the *cuboctahedral manifold*. The cuboctahedral manifold has 12 toric cusps, one for each ideal vertex of P_0.

We now completely determine the topology of W_t in the last interval $(0, t_2)$, as anticipated in Remark 4.12.

Proposition 4.13 *When $t \in (0, t_2)$, the manifold W_t is diffeomorphic to $C \times S^1$.*

Proof When $t \in (0, t_2)$, we see from Figure 14 that the four positive walls of the same parity (say odd, hence $\mathbf{1^+}$, $\mathbf{3^+}$, $\mathbf{5^+}$ and $\mathbf{7^+}$) intersect in a vertex v of P_t whose link is a regular tetrahedron with dihedral angles θ; there are two vertices like that — see Proposition 3.16(4).

We now consider these four positive walls altogether as a single wall Q, pleated along some faces; Figure 22 shows that Q is a cuboctahedron, pleated along six red pentagons with pleating angle θ. Since we are interested only in the topology of W_t, we may ignore the pleating (that is, we pretend that $\theta = \pi$).

Combinatorially, the polytope P_t is isomorphic to the prism $Q \times I$ over Q. The horizontal walls $Q \times \{0, 1\}$ are the two positive (even and odd) cuboctahedra. The lateral walls are

- the 6 letter walls, which are prisms over the ideal quadrilaterals of Q, and
- the 8 negative walls, which are prisms over the ideal triangles.

(Remember that we ignore the pleats and treat two faces of a wall adjacent along a red edge as the same face). The manifold W_t is obtained from $Q \times I$ via the colouring technique and is hence diffeomorphic to $C \times S^1$. □

Now, recall the fixed cuboctahedron $P_0 = P_t \cap \mathbb{H}^3$ described at the end of Section 3.4. As $t \to 0$, the nonright dihedral angles of P_t tend to π and the polytope collapses to the polyhedron P_0. Correspondingly, when the cone angles of the hyperbolic cone manifold W_t tend to 2π, the hyperbolic structure degenerates to that of the cuboctahedral manifold C, in a way that we now state precisely.

Let a *holonomy representation* of a hyperbolic cone manifold be a holonomy representation of its regular locus (the representation is unique up to conjugation). Here our construction furnishes for every $t \in (0, 1)$ a holonomy representation

$$\rho_t \colon \pi_1(W_t \backslash \Sigma_t) \to \mathrm{Isom}(\mathbb{H}^4).$$

Let $\rho\colon \pi_1(C) \to \mathrm{Isom}(\mathbb{H}^3) < \mathrm{Isom}(\mathbb{H}^4)$ be the faithful and discrete representation of the cuboctahedral manifold C.

Proposition 4.14 *As $t \to 0$, the representation ρ_t converges algebraically to a representation ρ_0 with $\mathrm{Im}(\rho_0) = \mathrm{Im}(\rho)$.*

Proof For every $g \in \pi_1(W_t \setminus \Sigma_t)$ the isometry $\rho_t(g)$ is a composition of reflections along the hyperplanes defining the polytope P_t.

As $t \to 0$, each halfspace $\mathbf{0^+}, \mathbf{0^-}, \ldots, \mathbf{E}, \mathbf{F}$ converges to some halfspace whose boundary hyperplane is either $\mathbb{H}^3$ or orthogonal to $\mathbb{H}^3$. This shows that $\rho_t(g)$ converges to a $\rho_0(g)$ contained in the image of ρ. By analysing the generators of $\pi_1(W_t \setminus \Sigma_t)$ we get $\mathrm{Im}(\rho_0) = \mathrm{Im}(\rho)$. $\qquad\square$

This degeneration is similar to the one famously described by Thurston [25], where a family of hyperbolic cone structures on a Seifert fibred manifold degenerates to the hyperbolic structure of the base orbifold as the cone angle approaches 2π.

The proof of Theorem 1.2 is complete.

The family is analytic

We remark that the deformation W_t is *analytic* in the following sense: the holonomy $\rho_t(\gamma)$ of an element $\gamma \in \pi_1(W_t \setminus \Sigma_t)$ varies analytically in t, because it is a product of reflections along hyperplanes dual to space-like vectors that vary analytically in t.

Note that the topology of $W_t \setminus \Sigma_t$ changes only at the critical times 1 and t_2. One can check that there is a natural embedding $\pi_1(W_{t_2-\varepsilon} \setminus \Sigma_{t_2-\varepsilon}) \hookrightarrow \pi_1(W_{t_2+\varepsilon} \setminus \Sigma_{t_2+\varepsilon})$, so the above definition actually makes sense also when t crosses t_2.

4.3 The deforming cone manifolds N_t

In the previous section we have constructed an interpolation between a manifold W_1 and an orbifold W_{t_1} through hyperbolic cone manifolds W_t with $t \in [t_1, 1]$, whose singular locus Σ is an immersed surface with varying cone angles. This interpolation is similar to the one required by Theorem 1.1, the main difference being that W_{t_1} is "only" an orbifold and not a manifold. In order to prove Theorem 1.1, in this section we now need to promote the orbifold W_{t_1} to a manifold. To do so, we construct a new manifold N_t by assembling some copies of P_t via a more complicated pattern than the one realising W_t.

The orbifold W_{t_1} contains a singular red surface (which consists of some punctured tori) with cone angle $\frac{2\pi}{3} = 2\theta$. We get this cone angle because every red quadrilateral in P_t has dihedral angle θ, and meets two copies of P_t in W_t. We now modify the construction of the previous section, so that each quadrilateral will meet six copies of P_t; this will make a total cone angle $6\theta = 2\pi$ at t_1 and hence the singularity will disappear.

To this purpose, we still use the P/N/L colouring of the walls of P_t, we still mirror P_t along N and L, but we glue the positive walls altogether with a more complicate pattern, that ensures that each red quadrilateral in the resulting complex has valence 6 instead of 2. This more complicate pattern is constructed by transposing into this context the famous triangulation of the figure-eight complement with two tetrahedra: the nice feature of this triangulation is that all edges have valence 6, and this is exactly what we need here.

The figure-eight knot pattern

We start by studying the symmetries of P_t.

Lemma 4.15 *For every bijection*

$$\sigma\colon \{1^+, 3^+, 5^+, 7^+\} \to \{0^+, 2^+, 4^+, 6^+\}$$

there exists a unique symmetry $s \in K$ of the polytope P_t such that $s(i) = \sigma(i)$ for every $i \in \{1^+, 3^+, 5^+, 7^+\}$ and for all $t \in (0, 1]$.

Proof Recall from Section 3.2 the group of symmetries K of P_t and its subgroup H. The group H acts on both sets $\{1^+, 3^+, 5^+, 7^+\}$ and $\{0^+, 2^+, 4^+, 6^+\}$ as their permutation group, and the roll symmetry R exchanges the two sets. □

Note that, when $t \in (t_1, 1)$, each positive wall is adjacent to all the other positive walls of the same parity and there are no triple intersections among positive walls; see Figure 11. Therefore, the four odd (resp. even) positive walls are arranged with the combinatorial pattern of a three-dimensional regular ideal tetrahedron: each wall corresponds to a face of the tetrahedron, while each red quadrilateral (intersection of two walls) corresponds to an edge of the ideal tetrahedron.

Consider the two ideal regular tetrahedra of Figure 23. We identify each four-tuple of walls

$$\{1^+, 3^+, 5^+, 7^+\}, \quad \{0^+, 2^+, 4^+, 6^+\}$$

with the faces of the left and right ideal tetrahedron, as shown in the figure.
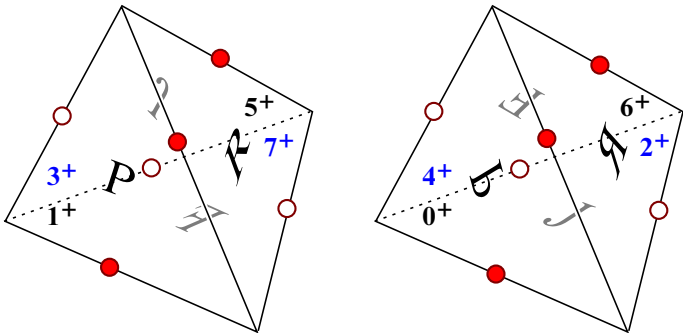
Figure 23: This is the ideal triangulation of the figure eight knot complement. We identify the odd (even) positive walls with the four faces of the left (right) tetrahedron, as shown here. Front faces are labelled in black and back faces in blue. The two resulting edges of the triangulation have valence six and are dotted in red and white.

The letters F, J, P, R in the figure determine a well-known face-pairing of the two tetrahedra: this is the face-pairing giving rise to the ideal triangulation of the figure-eight knot complement. It has the following nice combinatorial features:

- Each edge in the resulting combinatorial triangulation has valence 6.
- The return maps around the two edges are trivial.

The face-pairing of Figure 23 induces a wall-pairing

$$S = \{s_{\mathbf{1}+}, s_{\mathbf{3}+}, s_{\mathbf{5}+}, s_{\mathbf{7}+}\}$$

between the odd and even positive walls of P_t. Each s_i is an isometry from i to some even positive wall, determined as follows. Every $i \in \{\mathbf{1}^+, \mathbf{3}^+, \mathbf{5}^+, \mathbf{7}^+\}$ corresponds to a face of the left tetrahedron, which is glued to some face of the right one according to the pattern shown in Figure 23. The gluing extends to a unique isometry between the two tetrahedra, which induces a bijection

$$\sigma \colon \{\mathbf{1}^+, \mathbf{3}^+, \mathbf{5}^+, \mathbf{7}^+\} \to \{\mathbf{0}^+, \mathbf{2}^+, \mathbf{4}^+, \mathbf{6}^+\}.$$

The bijection in turns determines a symmetry s_i of P_t by Lemma 4.15, that restricts to an isometry between i and $\sigma(i)$. Note that the face-pairing S glues the wall G to H exactly with the pattern of Figure 23.

For instance, the symmetry $s_{\mathbf{1}+}$ sends $\mathbf{1}^+$ to $\mathbf{0}^+$ (the two faces in Figure 23 have the same letter P), and by looking at the orientation of the letter P we also see that $s_{\mathbf{1}+}$

acts as follows:

$$3^+ \to 4^+, \quad 7^+ \to 6^+, \quad 5^+ \to 2^+.$$

This determines the isometry s_{1+} between the walls $\mathbf{1}^+$ and $\mathbf{0}^+$. Following this recipe, it is not difficult to check that the wall-pairings in S are restrictions of the following isometries of $\mathbb{H}^4$ and symmetries of P_t:

$$s_{\mathbf{1}+}\colon (x_0, x_1, x_2, x_3, x_4) \mapsto (x_0, x_3, x_1, -x_2, -x_4),$$
$$s_{\mathbf{3}+}\colon (x_0, x_1, x_2, x_3, x_4) \mapsto (x_0, x_2, x_3, -x_1, -x_4),$$
$$s_{\mathbf{5}+}\colon (x_0, x_1, x_2, x_3, x_4) \mapsto (x_0, -x_3, x_1, x_2, -x_4),$$
$$s_{\mathbf{7}+}\colon (x_0, x_1, x_2, x_3, x_4) \mapsto (x_0, x_2, -x_3, x_1, -x_4).$$

Note that all such symmetries are orientation-preserving. This implies that the resulting cone manifold N_t (defined in the following paragraph) will *not* be orientable.

The manifolds N_t

Finally, we are ready to define the desired cone manifold N_t.

Definition 4.16 Let N_t be the hyperbolic cone manifold obtained by picking four copies P_t^{ij} for $i, j \in \{0, 1\}$ of the polytope P_t and by pairing their walls as follows:

(1) Identify every L wall in P_t^{0j} with the corresponding wall in P_t^{1j}.

(2) Identify every N wall in P_t^{i0} with the corresponding wall in P_t^{i1}.

(3) Identify the P walls in P_t^{ij} in pairs via the wall-pairing S.

In (1) and (2) we identify the corresponding walls using the identity map. We do the identifications (1), (2) and (3) for all $i, j \in \{0, 1\}$.

The hyperbolic cone manifold N_t is defined for all $t \in (0, 1]$, but we will be interested essentially in the interval $[t_1, 1]$.

The idea lying behind this construction is that everything should work locally like with W_t, except that now every red quadrilateral is incident to six copies of P_t instead of two and hence N_{t_1} will be a manifold and not an orbifold. We now analyse N_t carefully.

The singular set Σ

As for W_t, we start by analysing the singular set Σ.

Proposition 4.17 *The singular set Σ of N_t is the union of the green and red faces of the four copies of P_t.*

Proof Let $x \in \partial P_t$ be a point that does not lie in a green or red face. The point x is contained in one, two or three walls that are pairwise at right angles and have distinct colours. Since the identifications of the walls L and N are just mirrors, and that of the walls P preserves the colourings L and N, one sees easily that x becomes a smooth point in N_t. $\square$

As for W_t, to understand the singular set Σ of N_t it suffices to analyse the green and red faces of P_t.

Proposition 4.18 *When $t \in (t_1, 1)$, the singular set Σ is a geodesically immersed surface $\Sigma = T_0 \cup T_0' \cup T_1$, the union of two disjoint red cone tori $T_0 \sqcup T_0'$ and a green cone torus T_1, with cone angles 6θ and 4φ, respectively, intersecting in four points. The three tori have trivial normal bundles.*

Proof To understand Σ, we analyse all the finite vertices v in P_t and determine the unit tangent space of their images in N_t, as in the proof of Proposition 4.3. We refer to Figure 17.

By Proposition 3.13 there are two types of vertices v to analyse, with spherical link $\Delta = I_{\pi/2} * I_\theta$ or $I_\varphi * I_\theta$. The two types are considered similarly, so we only focus on $I_\varphi * I_\theta$. The four faces of Δ are coloured as P, P, N, L. After mirroring along negative walls, the link becomes $I_{2\varphi} * I_\theta$ and then, mirroring along the letter walls, we get a link $C_{4\varphi} * I_\theta$.

The join $C_{4\varphi} * I_\theta$ has two "faces" coloured as P, each isometric to a spherical disc with a cone point 4φ in its centre, tessellated into four triangles. In contrast to W_t, the P faces here are not doubled: they are paired according to the pattern of Figure 23. Since every edge has valence 6 in this pattern, 6 copies of $C_{4\varphi} * I_\theta$ are glued cyclically. Since the return map around every edge in Figure 23 is the identity (and not an edge reversal), the 6 copies are glued cyclically also with a trivial return map, giving rise to $C_{4\varphi} * C_{6\theta}$.

We have discovered that the link of v is $S^1 * C_{6\theta}$ or $C_{4\varphi} * C_{6\theta}$, according to the vertex type. We deduce that Σ is an immersed geodesic surface, made up of embedded orthogonal red and green surfaces having cone angles 6θ and 4φ.

A simple analysis on the topology of Σ shows that it consists of:

- Two red cone tori as in Figure 20, bottom-left, each with two cone points of angle 4φ, as we had in W_t.

- One green cone torus with four cone points of angle 6θ, which decomposes into eight green equilateral triangles like the single torus cusp section of the figure-eight knot complement triangulation in Figure 23.

It is also quite easy to check that their normal bundles are trivial. □

Corollary 4.19 *When $t \in [t_1, 1]$, the family N_t interpolates analytically between two cusped hyperbolic manifolds N_1 and N_{t_1}.*

Proof The cone manifolds N_1 and N_{t_1} have no singularities, since 4φ and 6θ are either 0 or 2π for these values. □

In the interpolation, the red tori are drilled at $t = 1$ and the green tori are drilled at $t = t_1$, producing new cusps.

The cusps

We now study the cusps of N_t.

Proposition 4.20 *The cone manifold N_t has*

- *three cusps at $t = t_1$,*
- *two cusps when $t \in (t_1, 1)$,*
- *four cusps at $t = 1$.*

The section of each cusp is a flat three-torus.

Proof We refer to Figure 18 for the links of the ideal vertices of P_t.

For $t \in (t_1, 1)$, consider the 12 ideal vertices v of P_t. The link of v is a parallelepiped with faces coloured in P, N, L. Recall that opposite faces share the same colour, and if their colour is P or N, then they have opposite parity. By mirroring the parallelepiped along N and L we get $S^1 \times S^1 \times I$. The pairing of the P faces then form some cycles. Each cycle gives a cusp and is a flat mapping torus with fibre $S^1 \times S^1$.

We now determine these cycles and the resulting mapping tori. We denote the 12 parallelepipeds as

$$C_{01}, \; C_{21}, \; C_{61}, \; C_{03}, \; C_{23}, \; C_{43}, \; C_{05}, \; C_{45}, \; C_{65}, \; C_{27}, \; C_{47}, \; C_{67},$$

where C_{ij} is the link of the ideal vertex of P_t adjacent to the four numbered walls $i^\pm$ and $j^\pm$ (and two letter walls; see Proposition 3.13). A computation shows that there

are two cycles,

$$C_{01} \cup_{s_{1+}} C_{03} \cup_{s_{3+}} C_{23} \cup_{s_{3+}} C_{27} \cup_{s_{7+}} C_{45} \cup_{s_{5+}} C_{61} \cup_{s_{1+}} C_{01},$$

$$C_{05} \cup_{s_{5+}} C_{65} \cup_{s_{5+}} C_{67} \cup_{s_{7+}} C_{47} \cup_{s_{7+}} C_{43} \cup_{s_{3+}} C_{21} \cup_{s_{1+}} C_{05}.$$

Therefore there are two cusps. The fact that each cycle has an even number of elements implies that both cusp sections are three-tori. Indeed, each s_i glues the odd P rectangle of a parallelepiped to the even P rectangle of the subsequent one; the opposite edges of each such rectangle are both coloured in N or L, and s_i preserves the colouring but exchanges the parity of N; it also inverts the natural orientation of the rectangle; however, since we compose an even number 6 of them, we get a mapping torus with monodromy $\left(\begin{smallmatrix} -1 & 0 \\ 0 & 1 \end{smallmatrix} \right)^6 = \left(\begin{smallmatrix} 1 & 0 \\ 0 & 1 \end{smallmatrix} \right)$.

The additional cusps are obtained by drilling tori having trivial normal bundles, therefore they are also of three-torus type.   □

Remark 4.21 We have here a third independent argument to show that $\mathrm{Vol}(P_{t_1}) = \mathrm{Vol}(P_1) = \frac{4\pi^2}{3}$, after Propositions 3.21 and 3.23. The manifold N_{t_1} is topologically obtained from N_1 by Dehn surgeries (first filling and then drilling along different tori), and these operations do not modify the Euler characteristic of a four-manifold. Therefore $\chi(N_{t_1}) = \chi(N_1)$, which implies $\mathrm{Vol}(N_{t_1}) = \mathrm{Vol}(N_1)$ and hence $\mathrm{Vol}(P_{t_1}) = \mathrm{Vol}(P_1)$.

Actually, an analogous reasoning could have been done in the previous section for W_1 and W_{t_1} in the orbifold context.

Remark 4.22 The hyperbolic manifold N_{t_1} contains a geodesic hypersurface diffeomorphic to the figure-eight knot complement. It comes from gluing together the walls **G** and **H** in P_t^{00}, which are regular ideal tetrahedra when $t = t_1$. This confirms the recent discovery that the figure-eight knot complement embeds geodesically [24].

The cone manifold W_t is tessellated into eight copies of P_t, while N_t is tessellated into only four. Therefore we have $\chi(N_1) = \chi(N_{t_1}) = 4$. (Recall that $\mathrm{Vol}(N) = \frac{4\pi^2}{3}\chi(N)$ for every hyperbolic 4–dimensional orbifold N.)

In the next section we will quotient N_t to a new cone manifold M_t and further cut the Euler characteristic by two.

Another Dehn filling

We only say few words on the cone manifolds N_t when $t < t_1$. We note that as soon as $t < t_1$ the cone angle 6θ is greater than 2π and N_t is not supported on a manifold

any more. Indeed, as soon as $t < t_1$, the topology of N_t changes from that of N_{t_1} by a Dehn filling that is different from the ones already considered and that was mentioned in the introduction: it consists of the collapsing of one $S^1 \times S^1$ factor in the $S^1 \times S^1 \times S^1$ shape of the cusp, which produces a small simple closed geodesic (as was mentioned in the introduction). This type of Dehn filling was already considered in [7; 8].

4.4 The manifolds M_t

The family N_t with $t \in [t_1, 0]$ is quite like the M_t required for proving Theorem 1.1, except that the singular set Σ contains two red tori instead of one and a green torus instead of a green Klein bottle (see Proposition 4.18). We now construct M_t as a quotient $M_t = N_t / \iota$, where ι is an appropriate fixed-point-free isometric involution that interchanges the two red tori (and the two cusps of M_t).

To construct ι, we exploit the well-known fact that the figure-eight knot complement has a fixed-point-free isometric involution ρ that permutes the two ideal tetrahedra in Figure 23 and the two edges, producing the nonorientable Gieseking manifold as a quotient (with a single tetrahedron and a single edge). Looking at Figure 23, the involution ρ sends the left tetrahedron to the right by acting on the faces as

$$1^+ \to 4^+, \quad 3^+ \to 6^+, \quad 5^+ \to 2^+, \quad 7^+ \to 0^+.$$

This corresponds to the isometric involution of P_t

$$r \colon (x_0, x_1, x_2, x_3, x_4) \mapsto (x_0, -x_1, -x_2, -x_3, -x_4).$$

The fact that ρ is an isometry of the figure-eight knot complement implies that ρ preserves the identifications of the faces in Figure 23, and this translates into the following equalities for r that one can verify directly, since $s_{7+} = s_{1+}^{-1}$, $s_{5+} = s_{3+}^{-1}$, and r commutes with them:

$$r = s_{7+} r s_{1+} = s_{5+} r s_{3+} = s_{3+} r s_{5+} = s_{1+} r s_{7+}.$$

These equalities say that r preserves the identification between the positive walls of P_t and, since r also preserves the N and L colours, it descends to an isometric involution $r \colon N_t \to N_t$ that acts as described on each copy P_t^{ij} of P_t.

The involution $r \colon N_t \to N_t$ has four fixed points: the four centres of the P_t^{ij} (there is no $x \in P_t$ that is identified with $r(x)$ through the wall-pairing S). To eliminate these fixed points, we define

$$\iota = h \circ r,$$

where h is the isometric involution of N_t that sends P_t^{ij} to $P_t^{1-i,1-j}$ via the identity map for each $i, j \in \{0, 1\}$. (The isometries h and r commute.) The isometry ι is fixed-point-free. Therefore the quotient $M_t = N_t/\iota$ is a hyperbolic cone manifold.

The involution ι exchanges the two red tori in the singular set of M_t, hence the singular set Σ of M_t contains a single red torus; it acts on the green torus as a fixed-point-free orientation-*reversing* involution, hence Σ also contains a green Klein bottle, tessellated into four equilateral green triangles like in a cusp section of the Gieseking manifold. (Similar to Remark 4.22, the hyperbolic manifold M_{t_1} contains a geodesically embedded copy of the Gieseking manifold.)

Proposition 4.23 *Both T and K have trivial normal bundle in M_t.*

Proof The tori T_0, T_0' and T_1 in N_t have trivial normal bundles. Therefore T does too, and the normal bundle of K is $(T_1 \times D^2)/\iota$, where ι sends (x, z) to $(i(x), -z)$. The resulting bundle is easily seen to be isomorphic to $K \times D^2$. $\qquad\square$

The proof of Theorem 1.1 is complete — it only remains to rescale and invert linearly the time parameter t from $[1, t_1]$ to $[0, 1]$.

4.5 Commensurability

We prove here the following:

Proposition 4.24 *The hyperbolic arithmetic four-manifolds M_0 and M_1 of Theorem 1.1 are not commensurable.*

Proof We first prove that the manifolds M_0 and M_1 are commensurable to the orbifolds P_1 and P_{t_1}, respectively (recall the time reparametrisation for M_t at the end of the last section).

The manifold M_0 is clearly commensurable with N_1. The manifold N_1 is constructed by gluing some identical copies of P_1 along some isometric pairings of their facets. The isometric pairings that we used are in fact all restrictions of some isometry of P_1, hence M_0 is a covering of the orbifold $P_1/\mathrm{Isom}(P_1)$ and therefore M_0 and P_1 are commensurable. The argument for M_1 and P_{t_1} is the same.

The thesis now follows from Proposition 4.25 below. $\qquad\square$

We now concentrate on the Coxeter polytopes P_1 and P_{t_1}, and actually on their quotients Q_1 and Q_{t_1}. We already know that they are both arithmetic, hence the manifolds M_0 and M_1 also are.

Recall that two subgroups $\Gamma_1, \Gamma_2 < \mathrm{Isom}(\mathbb{H}^n)$ are *commensurable* (in a wide sense) if there is a $g \in \mathrm{Isom}(\mathbb{H}^n)$ such that the intersection of $g^{-1}\Gamma_1 g$ and Γ_2 has finite index in both. This is an equivalence relation.

We briefly describe a procedure due to Maclachlan [16] to detect the commensurability class of any arithmetic hyperbolic reflection group $\Gamma < \mathrm{Isom}(\mathbb{H}^n)$ of finite covolume. We assume for simplicity that $n = 4$ and Γ is not cocompact (thus the field of definition is $\mathbb{Q}$). We also refer to [10, Section 4; 12, Section 5.1.2].

Notation and facts

We use the following notation:

- For $a, b \in \mathbb{Q}^*$, we denote by (a, b) the associated quaternion algebra over $\mathbb{Q}$.
- The symbol $\otimes$ is the tensor product over $\mathbb{Q}$.
- $\mathrm{Br}(\mathbb{Q})$ is the Brauer group of the field $\mathbb{Q}$.
- For a central simple $\mathbb{Q}$–algebra B, we let $[B] \in \mathrm{Br}(\mathbb{Q})$ be the Brauer equivalence class of B.

Recall that the Brauer group is an abelian group. The group operation is given by $[B_1] \cdot [B_2] = [B_1 \otimes B_2]$. In the Brauer group, the class of any quaternion algebra has order two. Vice versa, any order-two element of $\mathrm{Br}(\mathbb{Q})$ is represented by a quaternion algebra.

For any $\mathbb{Q}$–quaternion algebra B there are algorithms to compute its *ramification set*, which is a finite set of even cardinality whose elements are prime numbers or ∞. The ramification set is a complete invariant of the isomorphism class of B as a quaternion algebra. It is empty if and only if $B \simeq M_2(\mathbb{Q})$ if and only if $[B] = 1 \in \mathrm{Br}(\mathbb{Q})$.

Moreover, for any $\mathbb{Q}$–quaternion algebras B_1 and B_2, up to equivalence there exists a unique quaternion algebra B such that $[B_1] \cdot [B_2] = [B] \in \mathrm{Br}(\mathbb{Q})$. Hence, it makes sense to talk about the *ramification set* of $[B_1 \otimes B_2]$ as the ramification set of the quaternion algebra B. This set is the symmetric difference of the ramification sets of B_1 and B_2.

The commensurability classes of nonuniform arithmetic lattices of the Lie group $\mathrm{Isom}(\mathbb{H}^4)$ are in bijection with the isomorphism classes of quaternion algebras over $\mathbb{Q}$, which are classified by their ramification sets.

The algorithm

Given N *unit* space-like vectors $e_i \in \mathbb{R}^{1,4}$ for $i = 1, \ldots, N$ defining the reflection group Γ, the following algorithm gives a finite set of prime numbers or ∞ which characterises the commensurability class of Γ:

(1) Compute the Gram matrix $G = (g_{ij})_{ij}$ of Γ, that is, $g_{ij} = \langle e_i, e_j \rangle$.

(2) Determine all vectors of the form $v_{i_1,\ldots,i_k} = g_{1,i_1} g_{i_1,i_2} \cdots g_{i_{k-1},i_k} e_{i_k}$.

(3) The $\mathbb{Q}$–vector space $V = \mathrm{span}_{\mathbb{Q}}\{v_{i_1,\ldots,i_k}\}$ has dimension 5. Determine a $\mathbb{Q}$–basis $\mathcal{B} = \{v_1, \ldots, v_5\}$ of V.

(4) Consider the associated quadratic form q_G over V; it is of signature $(4, 1)$. Compute the matrix Q of the form q_G with respect to the basis $\mathcal{B}$. Diagonalise the form, to get a diagonal matrix $D = \mathrm{diag}(a_1, \ldots, a_5)$, with $a_i \in \mathbb{Q}^*$.

(5) Compute the Hasse invariant $s(q_G) = \left[\bigotimes_{i<j}(a_i, a_j)\right] \in \mathrm{Br}(\mathbb{Q})$ and the Witt invariant $c(q_G) = s(q_G) \cdot [(-1, -1)] \in \mathrm{Br}(\mathbb{Q})$.

(6) Compute the ramification sets of $s(q_G)$ and $c(q_G)$. To this aim, we will often use [10, Propositions 4.13 and 4.15].

We apply the algorithm to discover the following.

Proposition 4.25 *The* 24–*cell* P_1 *is commensurable with* $P_{\bar{t}}$ *and is* not *commensurable with* P_{t_1}.

Proof We apply the algorithm to the arithmetic Coxeter polytopes Q_1, Q_{t_1} and $Q_{\bar{t}}$. Recall that the vectors A, L, M, N are constant, in contrast with $\mathbf{0^+}$, $\mathbf{0^-}$, $\mathbf{3^+}$, $\mathbf{3^-}$, G, H, which depend on t.

We start with Q_1 and find

$$e_{0^+} = \left(1, \tfrac{\sqrt{2}}{2}, \tfrac{\sqrt{2}}{2}, \tfrac{\sqrt{2}}{2}, \tfrac{\sqrt{2}}{2}\right), \qquad e_{0^-} = \left(1, \tfrac{\sqrt{2}}{2}, \tfrac{\sqrt{2}}{2}, \tfrac{\sqrt{2}}{2}, -\tfrac{\sqrt{2}}{2}\right),$$
$$e_{3^+} = \left(1, \tfrac{\sqrt{2}}{2}, \tfrac{\sqrt{2}}{2}, -\tfrac{\sqrt{2}}{2}, -\tfrac{\sqrt{2}}{2}\right), \quad e_{3^-} = \left(1, \tfrac{\sqrt{2}}{2}, \tfrac{\sqrt{2}}{2}, -\tfrac{\sqrt{2}}{2}, \tfrac{\sqrt{2}}{2}\right),$$
$$e_G = \left(1, 0, 0, 0, -\sqrt{2}\right), \qquad\qquad e_H = \left(1, 0, 0, 0, \sqrt{2}\right),$$
$$e_A = \left(1, \sqrt{2}, 0, 0, 0\right), \qquad\qquad e_L = \left(0, -\tfrac{\sqrt{2}}{2}, \tfrac{\sqrt{2}}{2}, 0, 0\right),$$
$$e_M = \left(0, 0, -\tfrac{\sqrt{2}}{2}, \tfrac{\sqrt{2}}{2}, 0\right), \qquad\quad e_N = \left(0, 0, -\tfrac{\sqrt{2}}{2}, -\tfrac{\sqrt{2}}{2}, 0\right).$$

The Gram matrix is

$$G = \begin{bmatrix}
1 & 0 & -1 & 0 & -2 & 0 & 0 & 0 & 0 & -1 \\
0 & 1 & 0 & -1 & 0 & -2 & 0 & 0 & 0 & -1 \\
-1 & 0 & 1 & 0 & 0 & -2 & 0 & 0 & -1 & 0 \\
0 & -1 & 0 & 1 & -2 & 0 & 0 & 0 & -1 & 0 \\
-2 & 0 & 0 & -2 & 1 & -3 & -1 & 0 & 0 & 0 \\
0 & -2 & -2 & 0 & -3 & 1 & -1 & 0 & 0 & 0 \\
0 & 0 & 0 & 0 & -1 & -1 & 1 & -1 & 0 & 0 \\
0 & 0 & 0 & 0 & 0 & 0 & -1 & 1 & -\frac{1}{2} & -\frac{1}{2} \\
0 & 0 & -1 & -1 & 0 & 0 & 0 & -\frac{1}{2} & 1 & 0 \\
-1 & -1 & 0 & 0 & 0 & 0 & 0 & -\frac{1}{2} & 0 & 1
\end{bmatrix}.$$

We can choose $\mathcal{B} = (e_H, e_A, e_L, e_M, e_N)$, so that here Q is just a submatrix of G:

$$Q = \begin{bmatrix}
1 & -1 & 0 & 0 & 0 \\
-1 & 1 & -1 & 0 & 0 \\
0 & -1 & 1 & -\frac{1}{2} & -\frac{1}{2} \\
0 & 0 & -\frac{1}{2} & 1 & 0 \\
0 & 0 & -\frac{1}{2} & 0 & 1
\end{bmatrix}.$$

A diagonal form is $D = \mathrm{diag}(1, 1, -1, 1, 1)$, thus the Hasse invariant is trivial. We now turn to Q_{t_1} and find

$$e_{0+} = \left(\tfrac{\sqrt{3}}{2}, \tfrac{\sqrt{6}}{4}, \tfrac{\sqrt{6}}{4}, \tfrac{\sqrt{6}}{4}, \tfrac{\sqrt{10}}{4}\right), \quad e_{0-} = \left(\tfrac{\sqrt{5}}{2}, \tfrac{\sqrt{10}}{4}, \tfrac{\sqrt{10}}{4}, \tfrac{\sqrt{10}}{4}, -\tfrac{\sqrt{6}}{4}\right),$$
$$e_{3+} = \left(\tfrac{\sqrt{3}}{2}, \tfrac{\sqrt{6}}{4}, \tfrac{\sqrt{6}}{4}, -\tfrac{\sqrt{6}}{4}, -\tfrac{\sqrt{10}}{4}\right), \quad e_{3-} = \left(\tfrac{\sqrt{5}}{2}, \tfrac{\sqrt{10}}{4}, \tfrac{\sqrt{10}}{4}, -\tfrac{\sqrt{10}}{4}, \tfrac{\sqrt{6}}{4}\right),$$
$$e_G = (\sqrt{5}, 0, 0, 0, -\sqrt{6}), \quad e_H = (\sqrt{5}, 0, 0, 0, \sqrt{6}),$$
$$e_A = (1, \sqrt{2}, 0, 0, 0), \quad e_L = \left(0, -\tfrac{\sqrt{2}}{2}, \tfrac{\sqrt{2}}{2}, 0, 0\right),$$
$$e_M = \left(0, 0, -\tfrac{\sqrt{2}}{2}, \tfrac{\sqrt{2}}{2}, 0\right), \quad e_N = \left(0, 0, -\tfrac{\sqrt{2}}{2}, -\tfrac{\sqrt{2}}{2}, 0\right).$$

The Gram matrix is

$$G = \begin{bmatrix}
1 & 0 & -1 & 0 & -\sqrt{15} & 0 & 0 & 0 & 0 & -\frac{\sqrt{3}}{2} \\
0 & 1 & 0 & -1 & -1 & -4 & 0 & 0 & 0 & -\frac{\sqrt{5}}{2} \\
-1 & 0 & 1 & 0 & 0 & -\sqrt{15} & 0 & 0 & -\frac{\sqrt{3}}{2} & 0 \\
0 & -1 & 0 & 1 & -4 & -1 & 0 & 0 & -\frac{\sqrt{5}}{2} & 0 \\
-\sqrt{15} & -1 & 0 & -4 & 1 & -11 & -\sqrt{5} & 0 & 0 & 0 \\
0 & -4 & -\sqrt{15} & -1 & -11 & 1 & -\sqrt{5} & 0 & 0 & 0 \\
0 & 0 & 0 & 0 & -\sqrt{5} & -\sqrt{5} & 1 & -1 & 0 & 0 \\
0 & 0 & 0 & 0 & 0 & 0 & -1 & 1 & -\frac{1}{2} & -\frac{1}{2} \\
0 & 0 & -\frac{\sqrt{3}}{2} & -\frac{\sqrt{5}}{2} & 0 & 0 & 0 & -\frac{1}{2} & 1 & 0 \\
-\frac{\sqrt{3}}{2} & -\frac{\sqrt{5}}{2} & 0 & 0 & 0 & 0 & 0 & -\frac{1}{2} & 0 & 1
\end{bmatrix}.$$

We can choose $\mathcal{B} = (\sqrt{5}e_H, e_A, e_L, e_M, e_N)$, to get

$$Q = \begin{bmatrix} 5 & -5 & 0 & 0 & 0 \\ -5 & 1 & -1 & 0 & 0 \\ 0 & -1 & 1 & -\frac{1}{2} & -\frac{1}{2} \\ 0 & 0 & -\frac{1}{2} & 1 & 0 \\ 0 & 0 & -\frac{1}{2} & 0 & 1 \end{bmatrix}.$$

A diagonal form is $D = \mathrm{diag}(5, -1, 3, 1, 1)$. Thus, the Hasse invariant is

$$[(5, -1)] \cdot [(5, 3)] \cdot [(-1, 3)] = [(5, -3)] \cdot [(-1, 3)].$$

The ramification points of $[(5, -3)]$ and $[(-1, 3)]$ are $\{3, 5\}$ and $\{2, 3\}$, respectively; hence, the ramification points of the product are $\{2, 5\}$ and hence the element is nontrivial in the Brauer group $\mathrm{Br}(\mathbb{Q})$.

We finally look at $Q_{\bar{i}}$ and find

$$e_{0^+} = \big(\tfrac{\sqrt{2}}{2}, \tfrac{1}{2}, \tfrac{1}{2}, \tfrac{1}{2}, \tfrac{\sqrt{3}}{2}\big), \quad e_{0^-} = \big(\tfrac{\sqrt{6}}{2}, \tfrac{\sqrt{3}}{2}, \tfrac{\sqrt{3}}{2}, \tfrac{\sqrt{3}}{2}, -\tfrac{1}{2}\big),$$

$$e_{3^+} = \big(\tfrac{\sqrt{2}}{2}, \tfrac{1}{2}, \tfrac{1}{2}, -\tfrac{1}{2}, -\tfrac{\sqrt{3}}{2}\big), \quad e_{3^-} = \big(\tfrac{\sqrt{6}}{2}, \tfrac{\sqrt{3}}{2}, \tfrac{\sqrt{3}}{2}, -\tfrac{\sqrt{3}}{2}, \tfrac{1}{2}\big),$$

$$e_A = (1, \sqrt{2}, 0, 0, 0), \quad e_L = \big(0, -\tfrac{\sqrt{2}}{2}, \tfrac{\sqrt{2}}{2}, 0, 0\big),$$

$$e_M = \big(0, 0, -\tfrac{\sqrt{2}}{2}, \tfrac{\sqrt{2}}{2}, 0\big), \quad e_N = \big(0, 0, -\tfrac{\sqrt{2}}{2}, -\tfrac{\sqrt{2}}{2}, 0\big).$$

The Gram matrix is

$$G = \begin{bmatrix} 1 & 0 & -1 & 0 & 0 & 0 & 0 & -\tfrac{\sqrt{2}}{2} \\ 0 & 1 & 0 & -1 & 0 & 0 & 0 & -\tfrac{\sqrt{6}}{2} \\ -1 & 0 & 1 & 0 & 0 & 0 & -\tfrac{\sqrt{2}}{2} & 0 \\ 0 & -1 & 0 & 1 & 0 & 0 & -\tfrac{\sqrt{6}}{2} & 0 \\ 0 & 0 & 0 & 0 & 1 & -1 & 0 & 0 \\ 0 & 0 & 0 & 0 & -1 & 1 & -\tfrac{1}{2} & -\tfrac{1}{2} \\ 0 & 0 & -\tfrac{\sqrt{2}}{2} & -\tfrac{\sqrt{6}}{2} & 0 & -\tfrac{1}{2} & 1 & 0 \\ -\tfrac{\sqrt{2}}{2} & -\tfrac{\sqrt{6}}{2} & 0 & 0 & 0 & -\tfrac{1}{2} & 0 & 1 \end{bmatrix}.$$

We can choose $\mathcal{B} = (\sqrt{3}e_{3^-}, \sqrt{2}e_A, \sqrt{2}e_L, \sqrt{2}e_M, \sqrt{2}e_N)$, to get

$$Q = \begin{bmatrix} 3 & 0 & 0 & -3 & 0 \\ 0 & 2 & -2 & 0 & 0 \\ 0 & -2 & 2 & -1 & -1 \\ -3 & 0 & -1 & 2 & 0 \\ 0 & 0 & -1 & 0 & 2 \end{bmatrix}.$$

A diagonal form is $D = \mathrm{diag}(3, 2, 2, -1, 2)$. Thus, the Hasse invariant is

$$[(3,2)]^3 \cdot [(3,-1)] = [(3,2)] \cdot [(3,-1)] = [(3,-2)] = [(3, 1-3)] = 1 \in \mathrm{Br}(\mathbb{Q}).$$

This completes the proof. □

References

[1] **D V Alekseevskij**, **E B Vinberg**, **A S Solodovnikov**, *Geometry of spaces of constant curvature*, from "Geometry, II", Encyclopaedia Math. Sci. 29, Springer (1993) 1–138 MR

[2] **E M Andreev**, *The intersection of the planes of the faces of polyhedra with sharp angles*, Mat. Zametki 8 (1970) 521–527 MR In Russian; translated in Math. Notes 8 (1970) 761–764

[3] **M Boileau**, **B Leeb**, **J Porti**, *Geometrization of 3–dimensional orbifolds*, Ann. of Math. 162 (2005) 195–290 MR

[4] **K Bromberg**, *Hyperbolic cone-manifolds, short geodesics, and Schwarzian derivatives*, J. Amer. Math. Soc. 17 (2004) 783–826 MR

[5] **D Cooper**, **C D Hodgson**, **S P Kerckhoff**, *Three-dimensional orbifolds and cone-manifolds*, MSJ Memoirs 5, Mathematical Society of Japan, Tokyo (2000) MR

[6] **D A Derevnin**, **A D Mednykh**, **M G Pashkevich**, *The volume of a symmetric tetrahedron in a hyperbolic and a spherical space*, Sibirsk. Mat. Zh. 45 (2004) 1022–1031 MR In Russian; translated in Sib. Math. J. 45 (2004) 840–848

[7] **K Fujiwara**, **J F Manning**, CAT(0) *and* CAT(−1) *fillings of hyperbolic manifolds*, J. Differential Geom. 85 (2010) 229–269 MR

[8] **K Fujiwara**, **J F Manning**, *Simplicial volume and fillings of hyperbolic manifolds*, Algebr. Geom. Topol. 11 (2011) 2237–2264 MR

[9] **H Garland**, **M S Raghunathan**, *Fundamental domains for lattices in (ℝ−)rank 1 semisimple Lie groups*, Ann. of Math. 92 (1970) 279–326 MR

[10] **R Guglielmetti**, **M Jacquemet**, **R Kellerhals**, *Commensurability of hyperbolic Coxeter groups: theory and computation*, preprint (2017) To appear on RIMS Kôkyûroku Bessatsu

[11] **C D Hodgson**, **S P Kerckhoff**, *Rigidity of hyperbolic cone-manifolds and hyperbolic Dehn surgery*, J. Differential Geom. 48 (1998) 1–59 MR

[12] **M Jacquemet**, *New contributions to hyperbolic polyhedra, reflection groups, and their commensurability*, PhD thesis, Université de Fribourg (2015) Available at http://doc.rero.ch/record/257511

[13] **S P Kerckhoff**, **P A Storm**, *From the hyperbolic 24–cell to the cuboctahedron*, Geom. Topol. 14 (2010) 1383–1477 MR

[14] **S Kojima**, *Deformations of hyperbolic 3–cone-manifolds*, J. Differential Geom. 49 (1998) 469–516 MR

[15] **A Kolpakov**, **B Martelli**, *Hyperbolic four-manifolds with one cusp*, Geom. Funct. Anal. 23 (2013) 1903–1933 MR

[16] **C Maclachlan**, *Commensurability classes of discrete arithmetic hyperbolic groups*, Groups Geom. Dyn. 5 (2011) 767–785 MR

[17] **R Mazzeo**, **G Montcouquiol**, *Infinitesimal rigidity of cone-manifolds and the Stoker problem for hyperbolic and Euclidean polyhedra*, J. Differential Geom. 87 (2011) 525–576 MR

[18] **C T McMullen**, *The Gauss–Bonnet theorem for cone manifolds and volumes of moduli spaces*, Amer. J. Math. 139 (2017) 261–291 MR

[19] **G Montcouquiol**, *On the rigidity of hyperbolic cone-manifolds*, C. R. Math. Acad. Sci. Paris 340 (2005) 677–682 MR

[20] **G Montcouquiol**, *Déformations Einstein infinitésimales de cones-variétés hyperboliques*, preprint (2006) arXiv

[21] **G D Mostow**, *Strong rigidity of locally symmetric spaces*, Annals of Mathematics Studies 78, Princeton Univ. Press (1973) MR

[22] **G Prasad**, *Strong rigidity of $\mathbb{Q}$–rank 1 lattices*, Invent. Math. 21 (1973) 255–286 MR

[23] **S Riolo**, **L Slavich**, *New hyperbolic 4–manifolds of low volume*, preprint (2017) arXiv

[24] **L Slavich**, *The complement of the figure-eight knot geometrically bounds*, Proc. Amer. Math. Soc. 145 (2017) 1275–1285 MR

[25] **W P Thurston**, *The geometry and topology of three-manifolds*, lecture notes, Princeton University (1979) Available at http://msri.org/publications/books/gt3m

[26] **W P Thurston**, *Shapes of polyhedra and triangulations of the sphere*, from "The Epstein birthday schrift" (I Rivin, C Rourke, C Series, editors), Geom. Topol. Monogr. 1, Geom. Topol. Publ., Coventry (1998) 511–549 MR

[27] **E B Vinberg**, *Hyperbolic groups of reflections*, Uspekhi Mat. Nauk 40 (1985) 29–66 MR In Russian; translated in Russian Math. Surveys 40 (1985) 31–75

[28] **H Weiss**, *Local rigidity of 3–dimensional cone-manifolds*, J. Differential Geom. 71 (2005) 437–506 MR

[29] **H Weiss**, *Global rigidity of 3–dimensional cone-manifolds*, J. Differential Geom. 76 (2007) 495–523 MR

Dipartimento di Matematica, Università di Pisa
Pisa, Italy

martelli@dm.unipi.it,   riolo@mail.dm.unipi.it